JM PAPERS

Turbulent flows over porous lattices: alteration of near-wall turbulence and pore-flow amplitude modulation

Seyed Morteza Habibi Khorasani[1,†], **Mitul Luhar**[2] **and Shervin Bagheri**[1]

[1]FLOW, Department of Engineering Mechanics, KTH Royal Institute of Technology,
SE-100 44 Stockholm, Sweden

[2]Department of Aerospace and Mechanical Engineering, University of Southern California,
Los Angeles, CA 90089 USA

Turbulent flows over porous lattices consisting of rectangular cuboid pores are investigated using scale-resolving direct numerical simulations. Beyond a certain threshold which is primarily determined by the wall-normal Darcy permeability, K_y, near-wall turbulence transitions from its canonical regime, marked by the presence of streak-like structures, to another marked by the presence of Kelvin–Helmholtz-like (K–H-like) spanwise-coherent structures. The threshold agrees well with that previously established in studies where permeable-wall boundary conditions had been used as surrogates for a porous substrate (Gómez-de Segura & García-Mayoral, *J. Fluid Mech.*, vol. 875, 2019, pp. 124–172). In the smooth-wall-like regime, none of the investigated substrates demonstrate any reduction in drag relative to a smooth-wall flow. At the permeable surface, a notable component of the flow is that which adheres to the pore geometry and undergoes modulation by the turbulent scales of motions due to the interaction mechanism described by Abderrahaman-Elena *et al.* (*J. Fluid Mech.*, vol. 865, 2019, pp. 1042–1071). Its resulting effect can be quantified in terms of an amplitude modulation (AM) using the approach of Mathis *et al.* (*J. Fluid Mech.*, vol. 628, 2009, pp. 311–337). This pore-coherent flow component persists throughout the porous substrate, highlighting the importance of a given substrate's microstructure in the presence of an overlying turbulent flow. This geometry-related aspect of the flow is not accounted for when continuum-based models for a porous medium or effective representations of them, such as wall boundary conditions, are used. The intensity of the AM effect is enhanced in the K–H-like regime and becomes strengthened with larger permeability. As a result, structured porous materials may be designed to exploit or mitigate these flow features depending upon the intended application.

† Email address for correspondence: smhk2@kth.se

S.M. Habibi Khorasani, M. Luhar and S. Bagheri

1. Introduction

The interaction between fluid flows and porous media has in recent years witnessed a notable increase in attention. This is owing to their wide-ranging practical applications from heat exchangers (Kuruneru *et al.* 2020) to nuclear reactors (Hassan & Dominguez-Ontiveros 2008) as well as their pronounced presence in geophysical flows (Kazemifar *et al.* 2021). They are also interesting from a purely flow physics perspective, particularly with regards to turbulent flows, as their permeable quality can lead to the alteration of turbulence at the interface of porous media (Manes, Poggi & Ridolfi 2011). The interactions in this interfacial flow region affect the transport processes occurring between the surface and subsurface flows, motivating the need to better understand them.

Early studies of turbulence over porous media were mainly concerned with the effect that a permeable surface had on the structure of the overlying turbulent flow. This was primarily motivated by the understanding that the effect of wall permeability is distinct from wall roughness, an observation made in the comparative experiments of Zagni & Smith (1976) and Manes *et al.* (2009). One of the early numerical efforts pursuing this line of inquiry was that of Breugem, Boersma & Uittenbogaard (2006) who conducted direct numerical simulations (DNS) of turbulent channel flow with a porous substrate on one side. They classified the substrates in terms of their permeability Reynolds number, $Re_K = \sqrt{K}u_\tau/\nu = \sqrt{K^+}$, and resolved the flow inside the porous region as a continuum using the volume-averaged Navier–Stokes equations to only recover the scales of motion which were larger than the characteristic pore dimensions. Their results demonstrated that for highly permeable cases ($\sqrt{K^+} \gg 1$), the canonical streaks and quasistreamwise vortices of near-wall turbulence cease to exist and are replaced by large cross-stream vortical structures. Other observations made were that the logarithmic region of the mean velocity profiles over permeable surfaces differed from that over impenetrable smooth walls, resulting in the von Kármán constant, κ, being different for the porous channels. Additionally, their results also demonstrated an apparent lack of outer-layer similarity. Using the same methodology as Breugem *et al.* (2006), similar observations were also made in the later work of Kuwata & Suga (2017) who did scale-resolving DNS using the lattice-Boltzmann method. The earlier experimental work of Manes *et al.* (2011), however, did not report similarly divergent values of κ, with the authors suggesting those reported by Breugem *et al.* (2006) could be attributable to the lack of inner–outer scale separation, which itself could be a low-Reynolds-number effect. While not the focus of their work, the experimental measurements of Kim *et al.* (2020) of turbulent flows over packed beds of spheres were consistent with that of Manes *et al.* (2011) in this regard. In the recent DNS study by Shahzad, Hickel & Modesti (2023) of turbulent flows over perforated plates at $Re_\tau = 500-2000$, all flow cases demonstrated outer-layer similarity and $\kappa \approx 0.39$, with the authors also suggesting that the κ discrepancy in the work of Breugem *et al.* (2006) being attributable to the low Reynolds number of that study. Recently, Chen & García-Mayoral (2023) examined outer-layer similarity of wall-bounded turbulence by doing DNS of turbulent flows over canopies at at $Re_\tau = 550-1000$. They demonstrated that the method for estimating κ used by Breugem *et al.* (2006) and Kuwata & Suga (2017) can result in κ values which are potentially misleading. The method of the latter authors relies upon forcing the linearity of the mean velocity profile in logarithmic coordinates by introducing a suitably large displacement length such that the diagnostic function of the

mean velocity exhibits a flat plateau region corresponding to $1/\kappa$. Chen & García-Mayoral (2023) remark that κ cannot be meaningfully defined for flows where $Re_\tau < 300$ due to the limited range of wall-normal coordinates which prevents a logarithmic region from manifesting. In this low-Reynolds-number range, the diagnostic function by default will not have a plateau region of constant $1/\kappa$ which would correspond to a logarithmic region. It is also affected by the wake region above it (Luchini 2018). Thus, Chen & García-Mayoral (2023) demonstrate that enforcing the appearance of a plateau without correcting for the wake behaviour could lead to physically misleading values of κ.

Concerning the flow inside porous substrates subject to an overlying turbulent flow, Breugem *et al.* (2006) observed the presence of velocity fluctuations beneath the surface and considered them to be motions induced by pressure fluctuations. Kuwata & Suga (2017) likewise attributed the subsurface velocity fluctuations to the strong pressure diffusion directed into the substrate and caused by the Kelvin–Helmholtz-like (K–H-like) cross-stream rollers. More recently, Kim *et al.* (2020) provided direct experimental evidence of amplitude modulation (AM) for turbulence over permeable walls, a possibility that was highlighted by Efstathiou & Luhar (2018) based on skewness measurements in turbulent boundary layers over porous foams. This latter aspect will be of significance when examining the flow in the substrate region.

Kuwata & Suga (2017) examined the significance of anisotropy in porous media comprised of cubic pores and having either one (K_y), two (K_y, K_z; K_x, K_y) or three (K_x, K_y, K_z) non-zero diagonal components in the permeability tensor. They showed that wall-normal permeability alone did not affect the overlying turbulent flow and the additional presence of streamwise or spanwise permeability is necessary for alterations to occur. This configuration is unlike the DNS of Jiménez *et al.* (2001), where a permeable-wall boundary condition was used to permit penetration of wall-normal velocity. Likewise, the DNS study by Shahzad *et al.* (2023) of turbulent flows over perforated plates – porous walls with only non-zero wall-normal permeability – demonstrated that such porous structures can lead to non-smooth-like flow. This seeming contradiction is attributable to the specific geometry used in the K_y-only porous DNS of Kuwata & Suga (2017), which shelters the overlying turbulent flow from any recirculation that would occur in the cavities of the porous structures and causes the flow to simply 'skim' over the pores. This limitation does not exist for the boundary condition of Jiménez *et al.* (2001), which implicitly models the permeable wall as if it were connected underneath to a plenum chamber. Further examination of anisotropic permeability was carried out in the DNS study by Gómez-de Segura & García-Mayoral (2019), where the effect of a permeable wall was incorporated using wall boundary conditions derived from the Darcy–Brinkman equation for modelling porous media flows. For highly streamwise-preferential configurations ($K_x \gg K_y$), it was shown that the wall-normal permeability is the principal component responsible for the breakdown of the near-wall streak cycle and the emergence of the cross-stream K–H-like structures observed by Breugem *et al.* (2006). The threshold marking the onset of this K–H-like regime was estimated to be $\sqrt{K_y}^+ \approx 0.4$, with the flow fully belonging to this regime beyond $\sqrt{K_y}^+ \approx 0.6$. In this regime, drag became degraded compared with smooth-wall turbulence. Reductions in drag, however, were demonstrated for cases where the wall-normal permeability was $\sqrt{K_y}^+ < 0.4$.

The purpose of this study is to more closely examine the interaction between porous substrates and turbulent flows, both in the vicinity of the permeable surface and inside the porous substrate. This is investigated numerically using DNS which resolves the scales of motion from the bulk flow down to the pore scale. The substrates examined span both
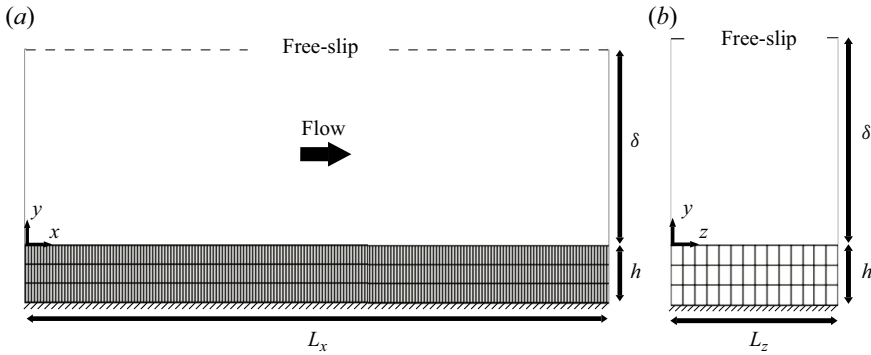
Figure 1. Sketch of the computational domain.

the canonical wall turbulence and K–H-like regimes. This allows for determining which aspects of the flow are mainly due to the change in turbulence and whether there are flow features which persist across both flow regimes, particularly in the substrates. The effect of surface geometry is also investigated.

The structure of the paper is as follows. In §2, the porous substrate geometries considered and their characteristics along with the numerical methods are introduced. How the overlying bulk turbulence becomes modified due to the presence of substrates and the resulting consequences in terms of drag are discussed in §3, where an assessment of outer-layer similarity and characterization of the bulk turbulence regime with respect to permeability is also described. In §4, the surface flow is examined to highlight the differences that exist in terms of flow structure over the substrates falling into different turbulence regimes. The flow in the substrates is examined in §5. The amplitude modulation of this flow by the overlying turbulence is discussed in §6. The results are summarized and discussed in §7.

2. DNS of turbulent flow over porous substrates

2.1. *Numerical method*

The configuration used in this study is an open-channel as depicted in figure 1. It is comprised of a bulk flow region with height δ and a porous substrate region of depth h. The direct numerical simulations using this set-up were conducted using the open-source solver PARIS simulator (Aniszewski *et al.* 2021) with in-house modifications. The code solves the incompressible Navier–Stokes equations,

$$\nabla \cdot \boldsymbol{u} = 0, \tag{2.1a}$$

$$\frac{\partial \boldsymbol{u}}{\partial t} + (\boldsymbol{u} \cdot \nabla)\,\boldsymbol{u} = -\frac{1}{\rho}\nabla p + \nu\nabla^2\boldsymbol{u}, \tag{2.1b}$$

where $\boldsymbol{u} = (u, v, w)$, p and ν are the velocity vector, pressure and kinematic viscosity, respectively. The velocity can be decomposed into its mean and fluctuating components through the Reynolds decomposition (Reynolds 1895)

$$\boldsymbol{u}(x, y, z, t) = \boldsymbol{U}(y) + \boldsymbol{u}'(x, y, z, t), \tag{2.2}$$

where $\boldsymbol{u}$ is the instantaneous velocity vector, $\boldsymbol{U}$ is the time- and plane-averaged mean velocity and $\boldsymbol{u}'$ is the fluctuating velocity varying over both space and time. Later on in

984 A63-4

this paper when examining the modulated flow inside the porous substrates, the further decomposition of u' into a time-steady and time-varying component (Reynolds & Hussain 1972)

$$u'(x, y, z, t) = \tilde{u}(x, y, z) + u''(x, y, z, t) \tag{2.3}$$

will also be used.

The dimensions of the computational domain are $(L_x, L_y, L_z) = (6.3\delta, 1.3\delta, 3.15\delta)$ in the streamwise (x), wall-normal (y) and spanwise (z) directions. The domain is periodic along x and z while being bounded by a free-slip surface at $y = \delta$ and a no-slip wall at $y = -0.3\delta$. The thickness of the porous substrate is $h = 0.3\delta$. The simulations were conducted at a constant mass flow rate, which was adjusted to target a nominal $Re_\tau = u_\tau \delta / \nu = 360$. Here, $u_\tau = \sqrt{\tau_w/\rho}$ is the friction velocity at $y = 0$ (the substrate surface), with τ_w obtained from the integral balance

$$\tau_w = -P_x \delta, \tag{2.4}$$

where P_x is the mean pressure gradient. Note that at $y = 0$, due to presence of a permeable surface τ_w will have contributions from both viscous and turbulent stresses,

$$\tau_w = \mu \frac{\mathrm{d}U}{\mathrm{d}y}\bigg|_{y=0} + \rho \overline{u'v'}|_{y=0}. \tag{2.5}$$

Throughout this paper, the superscript '+' indicates scaling in inner units, where quantities are normalized using u_τ and ν. The numerical grid has a resolution of $(N_x, N_y, N_z) = (1620, 324, 810)$. The grid spacing is uniform along x and z while being non-uniform along y. The grid is stretched in the region above the substrate using a hyperbolic tangent function and uniform within the substrate. The simulation results are grid independent at the chosen resolution. The grid independence was determined by conducting simulations at coarser and finer resolutions. The results of these simulations are gathered in Appendix A.

The equations are spatially discretized on a staggered Cartesian grid using central second-order finite differences. The fractional-step method (Kim & Moin 1985) is used to solve the discretized incompressible Navier–Stokes equations. At each time step an intermediate non-divergence free velocity field is first calculated. The Poisson equation obtained by imposing the incompressibility constraint is then solved using the fast-Fourier-transform-based solver of Costa (2018) to obtain the pressure correction. The pressure correction is then used to project the velocity field onto a divergence free vector space. The time integration uses a triple-substep Runge–Kutta method where both the advective and diffusive terms are treated explicitly.

The immersed boundary method of Breugem & Boersma (2005) is used to numerically realize the porous substrates. Unlike direct-forcing or penalization-based methods, it involves modifying the discretized advective and diffusive flux terms of the Navier–Stokes equations such that the no-slip and no-penetration conditions become exactly imposed for the regions of the numerical domain which are defined as solids. This makes it a more accurate method for realizing geometries which are Cartesian conforming, as demonstrated by Paravento, Pourquie & Boersma (2008).

In addition to the simulations including porous substrates, an open-channel flow over a smooth wall at $Re_\tau = 360$ was also simulated to serve as a baseline for comparisons. Quantities normalized using the smooth-wall friction velocity and kinematic viscosity are indicated by the subscript 'o'.
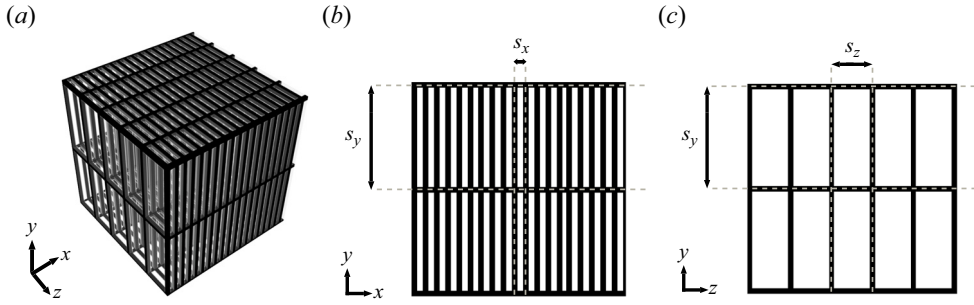
Figure 2. (*a*) Schematic of general substrate geometry along with (*b,c*) its nomenclature.

2.2. *Porous geometries*

The porous substrates investigated are lattices where the pores are repeating rectangular cuboids (figure 2). The solid matrix is made of rods with a cross-section of $d \times d$. The spacings (pitches) s_x, s_y and s_z determine the cross-sections of the pores and their resulting void volume. Consistent with previous experimental and numerical studies (Manes *et al.* 2011; Kuwata & Suga 2017; Gómez-de Segura & García-Mayoral 2019), the substrates are characterized in terms of their permeabilities obtained from Darcy's law (Darcy 1856),

$$u_D = -\frac{1}{\mu}\boldsymbol{K} \cdot \nabla p, \tag{2.6}$$

where $\boldsymbol{u}_D$ is the Darcy velocity vector, p is the pressure averaged over the fluid phase and $\boldsymbol{K}$ is the permeability tensor. As such, the law represents the balance between the pressure gradient that drives the flow through a porous medium and the resistance exerted by the medium's solid structure upon the flow. As the Darcy permeabilities are only dependent on the geometry of a substrate, they are suitable parameters for encapsulating the geometrical differences between different porous media. Similar to porous structures studied by Kuwata & Suga (2017), the Cartesian structure of the substrates makes the off-diagonal terms of the permeability tensor zero, giving a tensor with only the three diagonal components K_{xx}, K_{yy} and K_{zz}, which are written as K_x, K_y and K_z for simplicity. These components were computed from the results of Stokes flow simulations conducted using representative element volumes (REVs) of each substrate using the same solver that was used for the turbulent flow simulations. The dimensions of the REVs were $(L_x, L_y, L_z) = (0.3\delta, 0.3\delta, 0.3\delta)$ and the grid resolution similar to the turbulent simulations in terms of grid spacing. The inner-scaled lengths $\sqrt{K_x^+}$, $\sqrt{K_y^+}$ and $\sqrt{K_z^+}$ are used to characterize the porous substrates throughout the paper.

The main cases (HP1, HP2, HP3, MP, LP1, LP2, LP3) span a range of wall-normal permeabilities, $\sqrt{K_y^+}$, to facilitate investigating how near-wall turbulence becomes altered due to a progressively weakening wall-impedance. Here, HP designates higher permeability substrates ($\sqrt{K_y^+} > 2$), LP designates lower permeability substrates $\left(\sqrt{K_y^+} < 1\right)$ and MP a moderate permeability case falling between the other two groups $\left(1 < \sqrt{K_y^+} < 2\right)$. Cases HP2′ and HP3′ – where the wall-parallel spacings of HP2 and HP3 have been swapped – retain the wall-normal permeability of HP2 and HP3 but have increased streamwise permeability and hence anisotropy, $\Phi_{xy} = K_x/K_y$.

The simulation parameters along with the characteristics of their porous substrates are gathered in table 1. Representative elements for the HP and LP porous geometries

984 A63-6

Case	Symbol	Re_τ	φ	$s_{x_o}{}^+$	$s_{y_o}{}^+$	$s_{z_o}{}^+$	$\sqrt{K_{x_o}{}^+}$	$\sqrt{K_{y_o}{}^+}$	$\sqrt{K_{z_o}{}^+}$	Φ_{xy}
HP1	○	385	0.75	36.0	108.0	28.0	3.21	3.44	4.72	0.93
HP2	☆	373	0.68	36.0	54.0	28.0	2.74	2.62	3.84	1.05
HP3	◇	360	0.62	36.0	36.0	28.0	2.19	2.19	2.81	1.00
MP	○	359	0.50	28.0	27.0	28.0	1.50	1.53	1.50	0.98
LP1	☆	356	0.49	21.0	54.0	21.0	1.04	0.73	1.04	1.43
LP2	◇	359	0.39	21.0	36.0	21.0	0.91	0.62	0.91	1.47
LP3	□	359	0.26	21.0	21.0	21.0	0.50	0.50	0.50	1.00
HP2′	☆	378	0.68	28.0	54.0	36.0	3.84	2.62	2.74	1.47
HP3′	◇	361	0.62	28.0	36.0	36.0	2.81	2.19	2.19	1.28

Table 1. The DNS cases of open-channel turbulent flow over porous substrates. The porosity for each substrate is given by φ. The pore spacings are $s_{x_o}{}^+$, $s_{y_o}{}^+$ and $s_{z_o}{}^+$, while $\sqrt{K_{x_o}{}^+}$, $\sqrt{K_{y_o}{}^+}$ and $\sqrt{K_{z_o}{}^+}$ are the effective permeabilities, which are analogous to the permeability Reynolds number, Re_K. The ratio of streamwise to wall-normal permeability is Φ_{xy}. The rod or filament thickness of the solid matrix is $d/\delta = 0.039$ or $d_o{}^+ = 14$ for all cases. Labels, colours and symbols remain consistent throughout the manuscript.
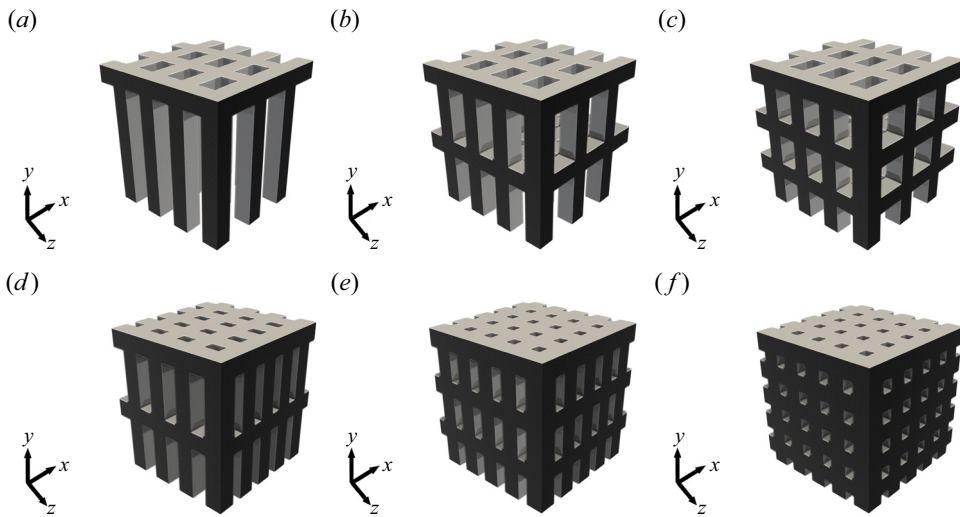

Figure 3. Representative elements of the LP and HP substrates in table 1. (*a*) HP1; (*b*) HP2; (*c*) HP3; (*d*) LP1; (*e*) LP2; (*f*) LP3. Cases HP2′ and HP3′ (not shown) are rotated versions of HP2 and HP3 around the *y* axis by $\pi/2$.

examined are shown in figure 3. The substrates will first be assessed with regards to certain aspects of permeable-wall turbulence which have been reported in the literature. This includes the transition of turbulence from the canonical near-wall regime to the K–H-like regime (Gómez-de Segura & García-Mayoral 2019) and the resulting drag changes. An important difference exists between pore-scale resolving simulations, and other simulation approaches such as volume-averaged Navier–Stokes simulations (Breugem *et al.* 2006; Rosti, Brandt & Pinelli 2018) and permeable-wall boundary conditions (Jiménez *et al.* 2001; Gómez-de Segura & García-Mayoral 2019). In the latter approaches, the permeability and porosity are predefined numerical parameters and independent from one another.
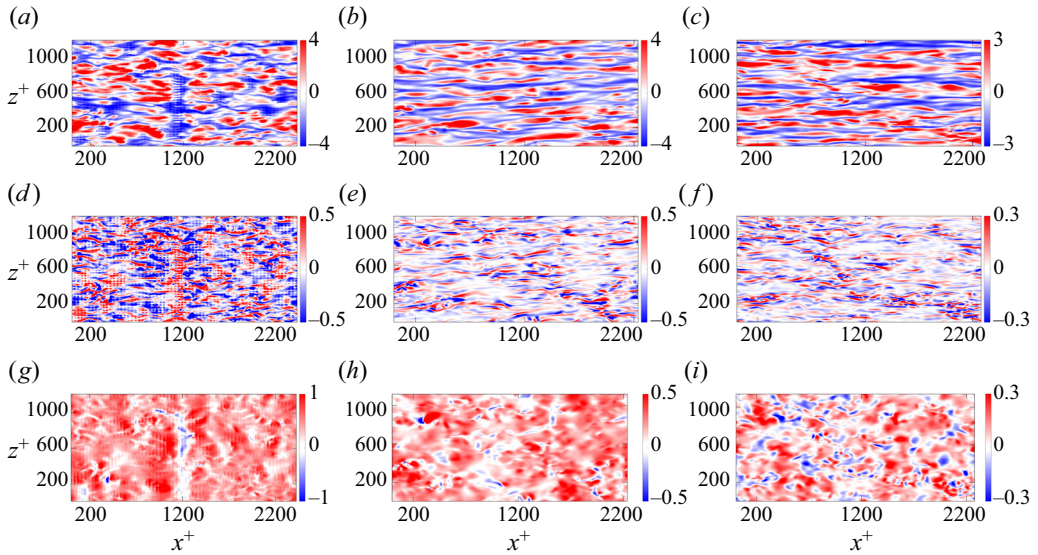
Figure 4. Instantaneous (*a–c*) streamwise velocity, (*d–f*) wall-normal velocity and (*g–i*) pressure fluctuations at $y^+ \approx 5$: (*a,d,g*) HP1; (*b,e,h*) LP1; (*c,f,i*) smooth-wall. Flow direction is from left to right.

For the cases considered in this work, the substrate's geometry determines both the permeability and the porosity. This imposes constraints on the permeabilities and the degree of anisotropy that can be obtained. For example, a change in s_x will change the pore cross-section along both y and z, leading to changes in K_y and K_z. The Reynolds numbers of DNS studies are also generally low relative to experiments. As such, achieving effective permeabilities ($\sqrt{K_x^+}$, $\sqrt{K_y^+}$, $\sqrt{K_z^+}$) which are large (such as those in Manes *et al.* (2011)) becomes challenging.

3. Overlying turbulent flow

3.1. *Surface region flow*

The changes in the overlying turbulent flow are first assessed qualitatively by examining the flow field above the permeable surface at $y^+ \approx 5$. Figure 4 shows instantaneous snapshots of the velocity and pressure fluctuations for HP1 and LP1. These two cases have the highest $\sqrt{K_y^+}$ of the HP and LP groups, respectively. This allows for a better assessment of the role wall impedance plays in causing changes in turbulence near the surface. Note that at the surface, the relevant permeability component is K_y as the flow must first be able to penetrate into the substrate before becoming redirected into the horizontal directions, for which K_x and K_z are important.

Beginning with observations for the streamwise velocity component, LP1 (figure 4*b*) exhibits regions of elongated positive and negative fluctuations which are similar to the streaky pattern observed over a smooth-wall (figure 4*c*). This streamwise coherency is diminished in HP1 (figure 4*a*), where the aforementioned regions are instead more clump-like and also exhibit a degree of regularity along the spanwise dimension of the domain. This is indicative of the near-wall turbulence becoming altered. For the wall-normal velocity component, the similarity between LP1 (figure 4*e*) and the smooth-wall (figure 4*f*) is reflective of the similarity seen in their streamwise velocity fields. Case LP1 has a greater degree of intensity but remains structurally similar to its
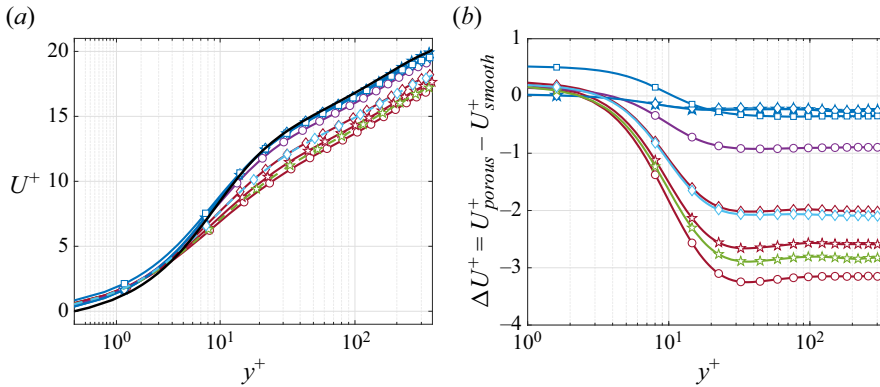
984 A63-8

Figure 5. (*a*) Mean velocity profiles of the bulk flow region above the porous substrates. (*b*) Difference in porous-wall and smooth-wall velocities. Symbols and colours follow the descriptions in table 1. The black line in (*a*) is a reference smooth-wall solution at $Re_\tau = 360$.

smooth-wall counterpart; HP1 (figure 4*d*), however, shows not only a noticeably stronger intensity in wall-normal velocity fluctuations but also structural differences, with there seemingly being an emergent spanwise coherency. The differences in the pressure fields are consistent with the observations made for the velocity fields. Case HP1 (figure 4*g*) demonstrates a spanwise patch along $x^+ \approx 1200$ which is coincident with the spanwise coherent regions seen at the same position in its u and v fields. The pressure fluctuations of HP1 are also more intense compared with LP1 (figure 4*h*) and the smooth-wall case (figure 4*i*). Another distinctive quality of HP1 is the visible signature of the permeable surface in its flow field, particularly when examining the wall-normal velocity (figure 4*d*). This indicates that the surface granularity becomes perceived by the turbulent flow, such that it leaves a visible footprint in the flow field. This is similar to what has been observed in flows over roughness (Abderrahaman-Elena, Fairhall & García-Mayoral 2019) and canopies (Sharma & García-Mayoral 2020).

3.2. *Changes in mean flow, velocity fluctuations and Reynolds shear stress*

Surfaces which depart from a hydrodynamically smooth behaviour change the overall level of momentum carried by the bulk flow, i.e. the amount of drag generated at the surface changes. As explained by Spalart & McLean (2011) and Chung *et al.* (2021), a suitable metric for quantifying this is the shift in the logarithmic region of the mean velocity profile, ΔU^+, which was introduced by Hama (1954) and Clauser (1954) and is more commonly known as the roughness function. As such, ΔU^+ accounts for the mean momentum deficit of the flow relative to smooth-wall flow. For the porous substrates, this is examined in figure 5(*a,b*), showing the mean velocity profiles, $U^+(y^+)$, and the velocity difference, $\Delta U^+(y^+) = U^+(y^+)_{porous} - U^+(y^+)_{smooth}$, respectively. All of the porous substrates examined increase drag compared with the baseline smooth-wall case ($\Delta U^+ < 0$), although the LP cases do not impose a significant drag penalty. The structural differences observed in the flow over the different substrates are also reflected here, such that they become distinguishable into two overall groups. The substrates with lower wall-normal permeability (LP1, LP2, LP3, MP) do not deviate greatly from the smooth-wall ($\Delta U^+ > -1$) and the LP cases are almost indistinguishable from the smooth-wall case. The substrates with higher wall-normal permeability (HP1, HP2, HP2′, HP3, HP3′) on the other hand result in ΔU^+ values which are notable ($\Delta U^+ \lesssim -2$). The
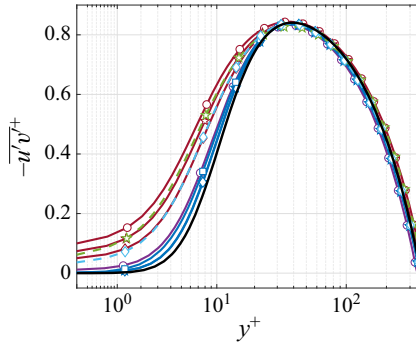
Figure 6. Reynolds shear-stress profiles of the bulk flow region above the porous substrates. The black line is a reference smooth-wall solution at $Re_\tau = 360$.

same distinction can be made for the Reynolds shear stress (figure 6), where substrates LP1, LP2, LP3 and MP result in slightly greater levels of turbulent activity close to the permeable surface whereas this activity is more pronounced for the HP substrates with a gap emerging between the former and the latter substrates in terms of their surface-level $-\overline{u'v'}^+$ activity.

Following the approach of MacDonald *et al.* (2016) and García-Mayoral, Gómez-de Segura & Fairhall (2019), to assess the contributing factors to ΔU^+, the mean momentum equation for the bulk flow region above the substrate is considered

$$\nu \frac{dU}{dy} - \overline{u'v'} = u_\tau^2 \left(1 - \frac{y}{\delta}\right). \tag{3.1}$$

Scaling (3.1) in inner units gives

$$\frac{dU^+}{dy^+} - \overline{u'v'}^+ = 1 - \frac{y^+}{\delta^+}. \tag{3.2}$$

Integrating (3.2) between $y^+ = 0$ (the substrate surface) and a position far above the substrate where the flow statistics are smooth-wall-like, $y^+ = H^+$, results in

$$\int_{y^+=0}^{y^+=H^+} -\overline{u'v'}^+ \, dy^+ + U^+\left(y^+ = H^+\right) - U^+\left(y^+ = 0\right) = H^+ - \frac{H^{+2}}{2\delta^+}. \tag{3.3}$$

For a smooth-wall flow, there will be no mean velocity at $y^+ = 0$ (no-slip) and hence $U^+(y^+ = 0) = U^+_{slip} = 0$. Taking the difference of (3.3) between a porous case and the smooth-wall case allows for quantifying the contributions of the interfacial slip velocity

984 A63-10

Case	κ	ΔU^+	ϵ^+	RMSE	R^2
Smooth-wall	0.39	0.00	0.0	0.04	0.99
HP1	0.39	−3.17	4.6	0.05	0.99
HP2	0.39	−2.52	4.2	0.05	0.99
HP3	0.39	−2.00	3.8	0.05	0.99
MP	0.39	−0.88	2.2	0.05	0.99
LP1	0.39	−0.27	1.3	0.07	0.99
LP2	0.39	−0.26	1.3	0.07	0.99
LP3	0.39	−0.34	0.9	0.06	0.99
HP2′	0.39	−2.76	2.6	0.02	0.99
HP3′	0.39	−2.08	2.3	0.05	0.99

Table 2. The von Kármán constant, κ, and virtual origin (or zero-plane displacement height), ϵ, resulting from the fitting of the log-law (3.5) to the mean velocity profiles of the different cases in table 1. The values of ΔU^+ for each case are also reported. The last two columns report the root mean square (r.m.s.) error and goodness of fit, respectively.

and changes in Reynolds stress to ΔU^+,

$$
\begin{aligned}
\Delta U^+ &= U^+ \left(y^+ = H^+ \right)_{porous} - U^+ \left(y^+ = H^+ \right)_{smooth} \\
&= U^+_{slip} - \int_{y^+=0}^{y^+=H^+} \left[\left(-\overline{u'v'}^+_{porous} \right) - \left(-\overline{u'v'}^+_{smooth} \right) \right] \mathrm{d}y^+ \\
&\quad - \frac{H^{+2}}{2} \left(\frac{1}{\delta^+_{porous}} - \frac{1}{\delta^+_{smooth}} \right) \\
&= \Delta U^+_{slip} + \Delta U^+_{uv} + \Delta U^+_{Re} \approx \Delta U^+_{slip} + \Delta U^+_{uv}.
\end{aligned}
\tag{3.4}
$$

The term ΔU^+_{Re} quantifies the contributions from additional turbulence scales and emerges due to the differences in Re_τ, i.e. δ^+_{porous} and δ^+_{smooth}. However, it remained negligible for the simulations conducted here and is therefore omitted. Note that differences in Re_τ would also result in non-zero ΔU^+_{Re} between smooth-wall flows and that this component is not due to the wall having a non-smooth characteristic.

The decomposition of (3.4) was applied to the different substrate cases by setting $H^+ = 200$, which measures ΔU^+ inside the region where it has achieved a flat value (figure 5b). Table 2 lists the corresponding ΔU^+ values for each configuration. The contributions obtained from (3.4) are shown in figure 7. There, it can be observed that the slip velocity contribution, ΔU^+_{slip}, to ΔU^+ does not vary significantly across the different cases. The Reynolds shear stress contribution, ΔU^+_{uv}, is drag degrading and hence always negative. The magnitude of ΔU^+_{uv} decreases monotonically from HP1, which has the overall highest permeability, to the LP cases which are similar in terms of ΔU^+. The dominant component across all cases is ΔU^+_{uv} and grows larger for substrates with greater wall-normal permeabilities. It is notably larger in magnitude than ΔU^+_{slip} for the HP cases. These results are consistent with what was observed for the profiles of the mean velocity (figure 5a) and Reynolds shear stress (figure 6). A jump in ΔU^+_{uv} is also seen here when going from the LP cases to the HP cases, suggestive of additional contributions resulting from the structural changes in turbulence that were observed in figure 4. The same trend holds for HP2′ and HP3′ which have weak streamwise-preferential anisotropy unlike their baseline counterparts HP2 and HP3. However, their increased anisotropy leads to increased
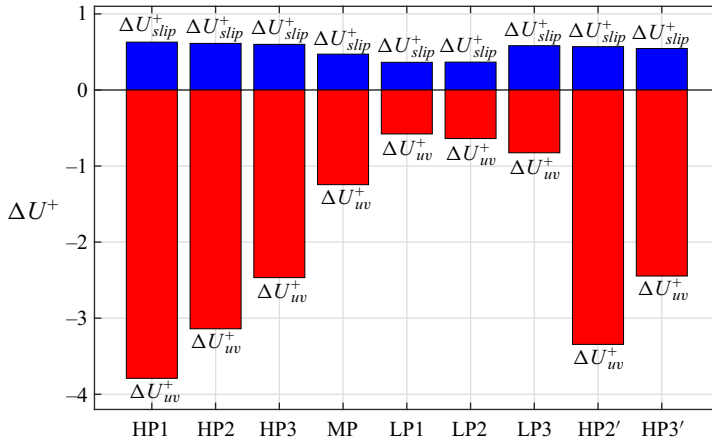
Figure 7. The slip velocity, ΔU_{slip}^+, and Reynolds shear stress, ΔU_{uv}^+, contributions to ΔU^+.

drag. In the LP cases on the other hand, as the anisotropy increases from LP3 to LP1 the drag becomes reduced, although the changes are small. Overall, none of the substrates allow for the development of any significant slip velocity at their surfaces. Therefore, the differences in ΔU^+ are primarily due to the differences in $-\overline{u'v'}^+$ close to the permeable surface.

The DNS of Gómez-de Segura & García-Mayoral (2019) where permeable-wall boundary conditions were used to effectively model anisotropic porous substrates suggested that streamwise-preferential configurations can result in drag reduction when turbulence is smooth-wall-like. Unfortunately, the mostly isotropic configurations of the substrates considered here do not permit investigating whether this applies to them. An earlier effort by the authors of this paper (Habibi Khorasani, Luhar & Bagheri 2022*a*) was directed towards this. The substrates used then were streamwise-preferential but still did not demonstrate drag reduction for those belonging to the smooth-wall-like turbulence regime. However, the flow in the porous region was weakly resolved due to the insufficient resolution of the simulations. A definitive conclusion could therefore not be made about drag reduction being achievable or not.

3.3. *Logarithmic law and outer-layer similarity*

Throughout the literature, assessments have been made about the applicability of the log-law, expressed as

$$U^+ = \frac{1}{\kappa}\ln\left(y^+\right) + B, \tag{3.5}$$

to non-smooth-wall flows. If the mean velocity of a non-smooth flow demonstrates a logarithmic scaling similar to a smooth-wall flow, the von Kármán constant, κ, should also be similar to the smooth-wall value. This similarity then also serves as an indicator that the two flows are outer-layer similar. When examining the log-law for non-smooth flows, a modified form of it,

$$U^+ = \frac{1}{\kappa}\ln\left(y^+ - \epsilon^+\right) + A + \Delta U^+, \tag{3.6}$$

is used instead. Here, A is the log-law intercept for a smooth-wall profile and ΔU^+ is the previously introduced mean velocity shift. Here ϵ^+ is the zero-plane displacement height

984 A63-12

or virtual origin and accounts for the differences in the origin of the logarithmic region. It therefore sets the location of the wall-normal coordinate origin, i.e. $y^+ = -\epsilon^+$. Different approaches have been used for determining ϵ^+. The method introduced by Jackson (1981) for rough-wall flows, where the virtual origin is associated with the centre of the drag forces acting on the rough wall, is a popular one. However, MacDonald *et al.* (2018) showed that a more suitable choice for ϵ^+ is the location at which the Reynolds shear stress, $\overline{u'v'}$, decays to zero. This definition of the virtual origin has also been used by Ibrahim *et al.* (2021) in their framework of quantifying drag changes for smooth-wall-like turbulence, where it accurately accounts for the turbulent contribution to drag. Using the same approach, for the porous substrates considered here, virtual origins are obtained that do not exceed a few wall units ($\epsilon^+ < 5$). The values of ϵ^+ are gathered in table 2. Comparing these values with the permeabilities of table 1, it is clear that the virtual origin is of the order of the permeabilities, with values close to $\sqrt{K_z^+}$. For permeable-walls which retain smooth-wall-like turbulence, ϵ has been shown to relate to the spanwise slip caused by the permeable substrate (Gómez-de Segura & García-Mayoral 2019), and the slip itself was shown by Abderrahaman-Elena & García-Mayoral (2017) to relate to $\sqrt{K_z^+}$ through analytical solutions of the Brinkman equation. However, it should be emphasized that this is only applicable to the viscous-dominated smooth-wall-like regime of drag change established in Luchini, Manzo & Pozzi (1991) and Luchini (1996). Additionally, the presence of tangential permeability is not necessary for slip to occur. This is evident from the DNS of Shahzad *et al.* (2023), who also reported $\epsilon^+ < 5$ but for acoustic liners where $\sqrt{K_x^+} = \sqrt{K_z^+} = 0$.

After determining ϵ^+, the values of κ were obtained by fitting (3.6) to the mean velocity profiles of each case. These values are gathered in table 2. $\kappa \approx 0.39$ across all cases which is the value commonly reported for smooth-wall turbulence. Similar to the virtual origins, this result also mirrors that of Shahzad *et al.* (2023). For the reasons described earlier in § 1, the approach of Breugem *et al.* (2006) has not been adopted to determine ϵ^+ and κ. The Reynolds number for the flows examined here is too low for the diagnostic function, $y^+ \, dU^+/dy^+$, to be reliably used. It should also be reiterated that the flow configuration used here is an open channel, whereas those of Breugem *et al.* (2006) and Kuwata & Suga (2017) were asymmetric confined channels. This undermines any direct comparisons. Regarding the κ values obtained in prior work and the choice of method to do so, the interested reader is referred to the work of Chen & García-Mayoral (2023) which directly deals with subjects of log-law analysis and outer-layer similarity in obstructed flows. The recent work of Luchini (2024) may also provide insight regarding log-laws in general.

Setting aside log-law behaviour, the similarity hypothesis of Townsend (1976) requires that the inner-scaled turbulent fluctuations be similar away from the wall. In figure 8, the r.m.s. velocity fluctuations (figure 8b) and Reynolds shear stress (figure 8a) distributions in outer-scaled wall-coordinates are similar beyond $y/\delta \approx 0.25$. This reflects figure 5(b), where ΔU^+ became flat beyond $y^+/Re_\tau \approx 0.25$. Therefore, the effect of the porous substrates does not extend far into the overlying flow, reinforcing the existence of outer-layer similarity.

3.4. *Flow regime distinction based on permeability*

The separation of the substrates into two groups becomes more clearly distinguishable when plotting the drag change, ΔU^+, against the square root of the wall-normal permeability (figure 9a). The leap in ΔU^+ when going from the LP to the HP cases
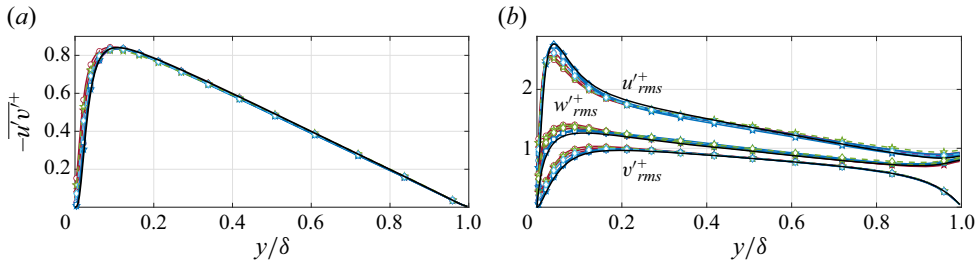
Figure 8. (*a*) Reynolds shear stress and (*b*) r.m.s. velocity fluctuations above the substrates in outer-scaled wall coordinates.

has been attributed to the near-wall turbulence dynamics undergoing a transition and departing the canonical regime for a K–H-like one (Gómez-de Segura & García-Mayoral 2019). Using linear stability analysis with boundary conditions derived from the Darcy–Brinkman equation, Gómez-de Segura, Sharma & García-Mayoral (2018) proposed the following relation for quantifying the influence of a substrate's permeability on triggering this transition:

$$K_{Br_1}^+ = K_y^+ \tanh\left(\frac{\sqrt{2K_x^+}}{9}\right) \tanh^2\left(\frac{h^+}{\sqrt{12K_y^+}}\right) \approx K_y^+ \tanh\left(\frac{\sqrt{2K_x^+}}{9}\right). \qquad (3.7)$$

For sufficiently deep substrates, the second hyperbolic tangent term becomes ≈ 1 and the relation becomes simplified, with the dominant term becoming K_y^+. Gómez-de Segura & García-Mayoral (2019) determined $\sqrt{K_{Br_1}^+} \approx 0.4 - 0.6$ as the threshold in which the onset and transition to the K–H-like regime occurs. The results of applying (3.7) to the DNS data in this work is shown in figure 9(*c*). It indicates that case MP and beyond should belong to the fully developed K–H-like regime, since $\sqrt{K_{Br_1}^+} \approx 0.68$ for MP. Cases HP2′ and HP3′, which differ in terms of their Φ_{xy} anisotropy from the other HP cases (figure 9*b*), also conform to (3.7). However, as will be shown later in § 3.5 through spectral analysis, case MP does not fall into the fully developed K–H-like regime, but does show evidence of the onset of the regime. It should be noted that (3.7) was originally obtained for conditions where $\sqrt{K_x^+} > \sqrt{K_y^+}$, i.e. streamwise-preferential substrates, therefore it may not be suitable for the substrates under consideration here. For conditions where $\sqrt{K_x^+} < \sqrt{K_y^+}$, Sharma *et al.* (2017) demonstrated that linear stability analysis leads to different results, described using

$$K_{Br_2}^+ = \sqrt{K_x^+ K_y^+} \tanh\left(\frac{h^+}{18}\sqrt{\frac{K_x^+}{K_y^+}}\right) \tanh^2\left(\frac{h^+}{\sqrt{K_x^+}}\right) \approx \sqrt{K_x^+ K_y^+}, \qquad (3.8)$$

where the hyperbolic tangent terms again become ≈ 1. The results from applying (3.8) to the simulation data of the cases in table 1 are shown in figure 9(*d*). They are similar to those in figure 9(*c*) obtained using (3.7). Anisotropy becomes reflected more prominently when characterizing the substrates using (3.8), as HP2′ and HP3′ become more separated from HP2 and HP3 in figure 9(*d*) compared with figure 9(*c*). Sharma *et al.* (2017) reported that for $\sqrt{K_{Br_2}^+} > 2$ the K–H-like instability becomes fully developed. For HP3, $\sqrt{K_{Br_2}^+} \approx 2.2$, and in § 3.5 it will be shown through spectral analysis that the HP cases belong to the K–H-like regime. As such, the instability criteria of Gómez-de Segura *et al.*
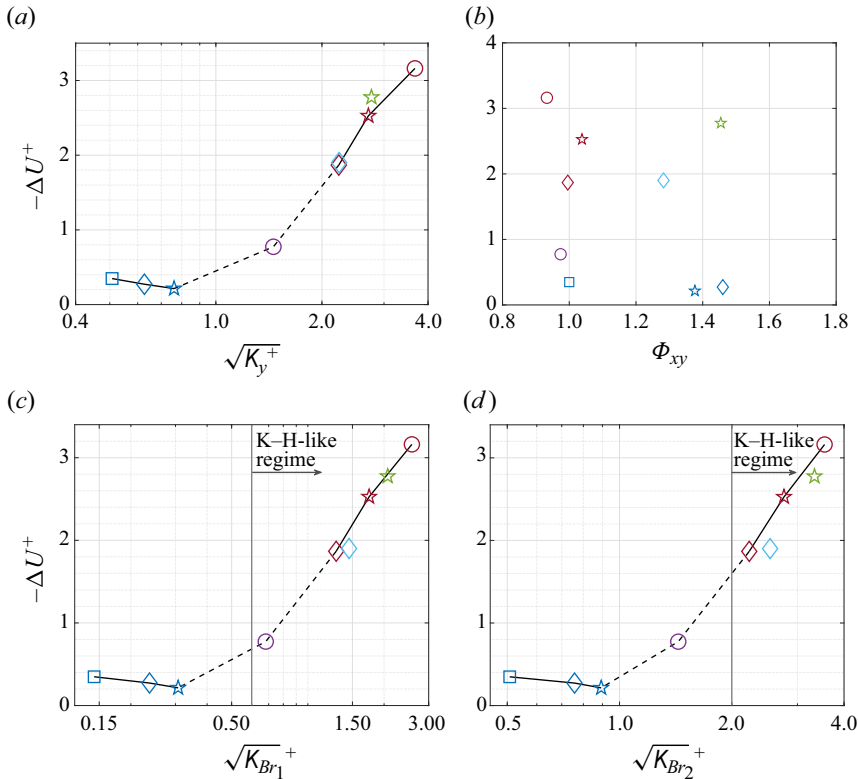
984 A63-14

Figure 9. Mean velocity shift plotted against (*a*) wall-normal permeability, (*b*) the streamwise to wall-normal anisotropy ratio, (*c*) effective permeability of (3.7) and (*d*) effective permeability of (3.8). Here □, blue, LP1; ◇, blue, LP2; ☆, blue, LP3; ◯, purple, MP; ◇, red, HP3; ☆, red, HP2; ◯, red, HP1; ◇, blue, HP3′; ☆, green, HP2′. The vertical lines mark the thresholds beyond which the cases are expected to fall into the fully developed K–H-like regime according to Gómez-de Segura & García-Mayoral (2019) and Sharma, Gomez-de Segura & Garcia-Mayoral (2017).

(2018) and Sharma *et al.* (2017) are good predictors of when the turbulence dynamics over porous structures cease to be canonical. The first-order influence of K_y^+ becomes evident when taking into account that the weakening of the wall-blocking effect at the surface is directly tied to this permeability component. Once permeability at the surface is present to a sufficiently large degree to permit the penetration of momentum into the substrate, the fluid moving below the surface must then contend with the horizontal blockage imposed by the substrate which is characterized by K_x^+ and K_z^+, giving these permeability components second-order significance. The two criteria of (3.7) and (3.8) will probably exhibit more distinguishable results from one another for substrates with higher anisotropy, whereas here they give results which are mostly similar to one another.

Earlier in the introduction, it was mentioned that the predominance of K_y^+ may seem to contradict the results of Kuwata & Suga (2017) for their porous structure which only had the K_y^+ permeability component but differed little from smooth-wall turbulence. This can be made more confusing when one considers the earlier work of Jiménez *et al.* (2001), where a permeability boundary condition was used to allow for wall transpiration and the resulting flows became K–H-like. For the case of Kuwata & Suga (2017), the lack of any wall-parallel permeability prevents flow from recirculating within the substrate. This has the effect of inhibiting wall transpiration since there is no room for the fluid to
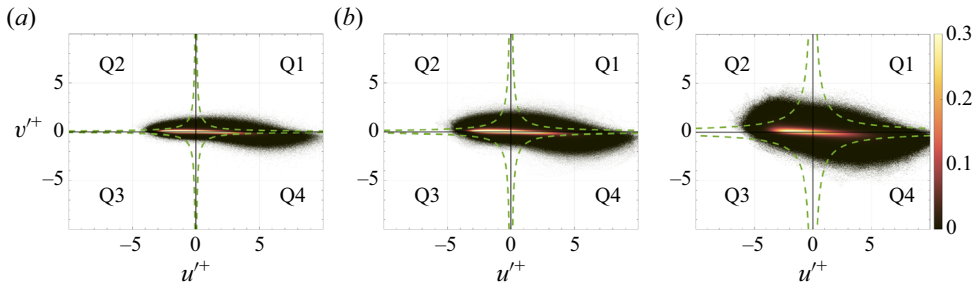
Figure 10. Quadrant maps of u' and v' at $y^+ \approx 5$: (*a*) smooth-wall, (*b*) LP1, (*c*) HP1. The dashed lines are hyperbolas marking $|u'^+ v'^+| = 8 \times -\overline{u'v'}^+$. The colour bar indicates the frequency of events in each bin of the map.

achieve recirculation underneath. This restriction does not exist for the boundary condition used by Jiménez *et al.* (2001), which implicitly assumes that the permeable wall has a plenum chamber underneath it. This is also the reason why the acoustic liners of Shahzad *et al.* (2023) demonstrate non-smooth-wall behaviour, despite only having K_y^+. The liners consist of arrays of cavities with a perforated lid on top of them. Each cavity has multiple orifices with diameters larger than 80 in wall units over it, making the cavity volume relatively large. Each cavity in effect then behaves as a plenum chamber where the fluid can recirculate.

3.5. *Turbulence structure*

In figure 6, it was shown that the HP cases are distinguished by higher Reynolds shear stresses in the region close to the permeable surface. Quadrant analysis of the velocity fluctuations can be leveraged to examine the change in turbulence intensities with respect to flow events, in particular the contribution from ejections (Q2, $u' < 0$ and $v' > 0$) and sweeps (Q4, $u' > 0$ and $v' < 0$). This is shown for the $y^+ \approx 5$ plane above the surface in figure 10. Going from an impenetrable smooth-wall (figure 10*a*) to the permeable case of LP1 (figure 10*b*) and finally the greater permeable case of HP1 (figure 10*c*), a tilting and expansion of the joint probability distributions of u' and v' is observed. As explained by Manes *et al.* (2011), the tilting is attributable to an increase in v' activity, which is also evident when viewing the r.m.s. velocity fluctuations in figure 11, particularly when going from the LP to the HP cases. In terms of flow events, sweeps become increasingly dominant as the permeability increases, in both strength and number of occurrences, contributing to a greater generation of Reynolds shear stress in the near-surface region. Structurally, the rounder distribution for the HP1 is also indicative of turbulence growing less anisotropic (Suga, Mori & Kaneda 2011). These features are common to flows over permeable surfaces, be they canopies (Finnigan, Shaw & Patton 2009) or porous media (Manes *et al.* 2011).

The experiments of Manes *et al.* (2011) also showed the distribution of points initially growing and then subsequently shrinking when going from their lowest permeability to their highest permeability case (refer to figure 15 of their manuscript). They attributed this behaviour to the near-surface flow mechanism changing to a mixing-layer type for the highest permeability porous media they investigated, similar to what occurs for turbulence over canopies (Finnigan 2000). The highest permeability examined by Manes *et al.* (2011), for which they observed mixing-layer behaviour, was $\sqrt{K^+} \approx 17$ at $Re_\tau \approx 3848$. This is
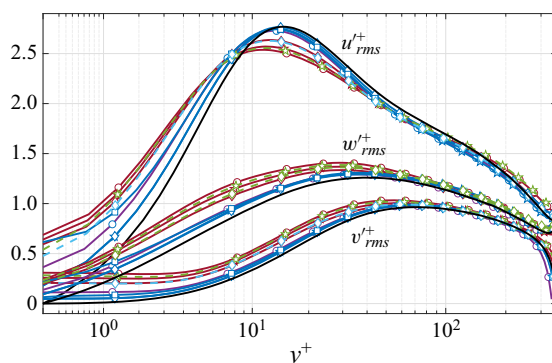
Figure 11. Distributions of the r.m.s. velocity fluctuations for the bulk turbulent flow overlying the porous substrates.

considerably greater than the highest effective wall-normal permeability investigated here ($\sqrt{K_y^+} \approx 3.4$), suggesting that the cases in this study do not fall into the category of mixing-layer type behaviour.

The differences in turbulence structure become better established by examining the spectral energy densities of the velocity fluctuations. The spectra of cases HP1 and LP1 in figure 12 are different from one another, with HP1 exhibiting energetic scales at large spanwise wavelengths which are absent in LP1. For case MP, the onset of the instability can be inferred from the emergence of energetic scales at large λ_z^+, but it is not yet intensified. This spanwise coherent component is attributable to the existence of spanwise rollers associated with a K–H-like instability over permeable boundaries (Gómez-de Segura & García-Mayoral 2019). A visualization of the vortical structures appearing in the HP cases is shown in figure 13. Additionally, by using spectral proper orthogonal decomposition (SPOD), modes are obtained for HP1 which capture the spanwise coherent rollers but for LP1, and indeed all of the LP cases, no such modes are obtained. These SPOD modes for HP1 may be viewed in Appendix B, but have been omitted from the main text for brevity. The emergence of these K–H-like structures is the cause behind the intensification of turbulent activity in the proximity of the substrate surface and drag increase.

Recalling the drag decomposition in figure 7, it was observed that increased streamwise-preferential anisotropy had a drag reducing effect in the LP cases, albeit a small one. As it is clear now that these cases belong to the smooth-wall-like turbulence regime, this makes the trend observed for drag change in line with the results of Gómez-de Segura & García-Mayoral (2019). In the smooth-wall-like regime, the changes in drag are due to the 'virtual-origin' effect (Luchini *et al.* 1991; Jiménez 1994; Luchini 1996; García-Mayoral *et al.* 2019; Ibrahim *et al.* 2021; Habibi Khorasani *et al.* 2022*b*), where the Reynolds shear stress generating quasistreamwise vortices can become displaced farther away from the surface where a slip velocity is present, resulting in a net drag reduction. This linear mechanism of passive drag reduction is only achievable so long as the flow surrounding the surface remains quasilaminar (Luchini 2015) and becomes negated beyond it. Owing to their smooth-wall-like quality, the drag components of LP1, LP2 and LP3 are likely quantifiable in terms of virtual origins using the approach of Ibrahim *et al.* (2021), but this has not been carried out here.
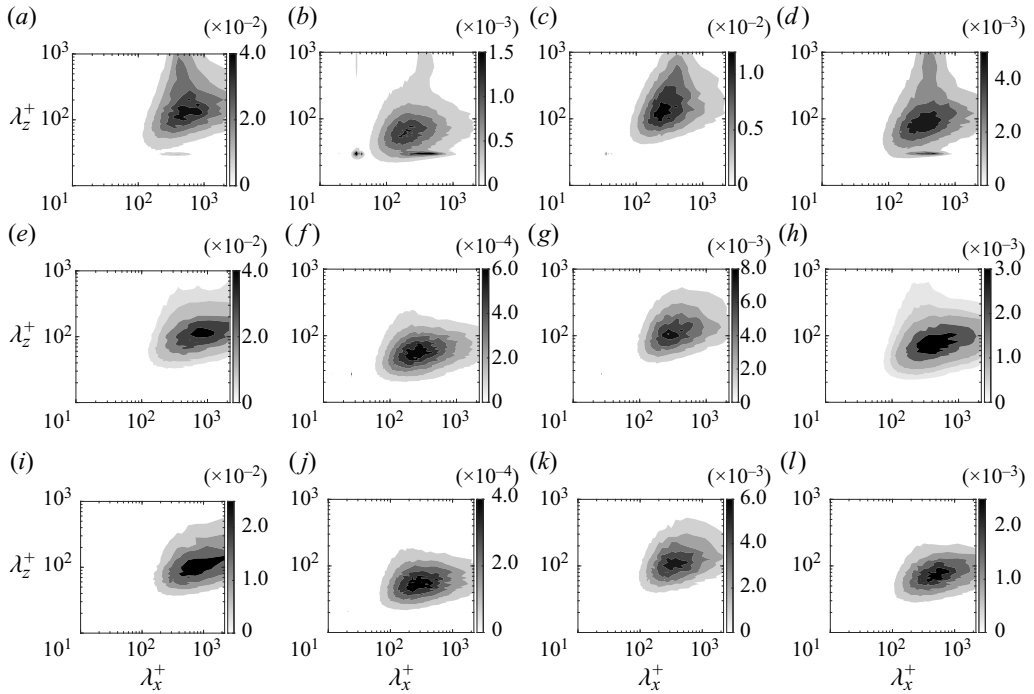
Figure 12. Premultiplied two-dimensional spectral energy densities: (a,e,i) $k_x k_z E_{uu}$; (b,f,j) $k_x k_z E_{vv}$; (c,g,k) $k_x k_z E_{ww}$; (d,h,l) $k_x k_z E_{uv}$ at $y^+ \approx 5$. Here $(a–d)$ HP1; $(e–h)$ MP; $(i–l)$ LP1.
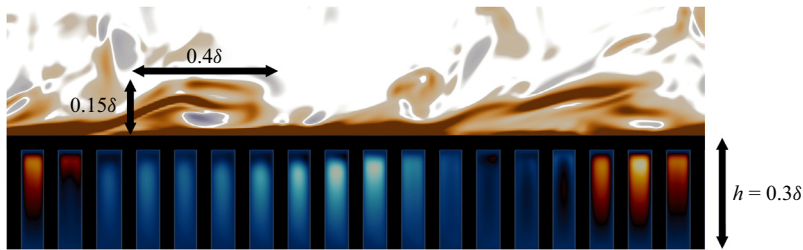

Figure 13. Vortex visualization using the Q-criterion above substrate HP1 in an x–y slice through the simulation domain. Vortex cores (light colour) are regions of $Q > 0$ (high vorticity) and surrounded by a sheet (dark colour) of $Q < 0$ (high shear). The hot and cold regions below the surface represent positive and negative wall-normal velocity fluctuations, respectively. Flow direction is from left to right.

4. Surface flow

The focus is now placed on the permeable surface of the substrates at $y^+ = 0$, which is the region directly in contact with the overlying turbulent flow. Figure 14 shows the velocity and pressure fluctuations at $y^+ = 0$; the differences that were observed in the flow fields of HP1 and LP1 above the surface (figure 4) are also reflected here. It can be observed from figure 14(a) that HP1 lacks the streaky patterns of LP1, shown in figure 14(b), but has more intense activity. The imprint of the surface geometry is also more clearly visible in the flow field of HP1. For the wall-normal velocity, spanwise coherent patterns are observable for HP1 (figure 14c) whereas such coherency is not discernible for LP1 (figure 14d).

984 A63-18
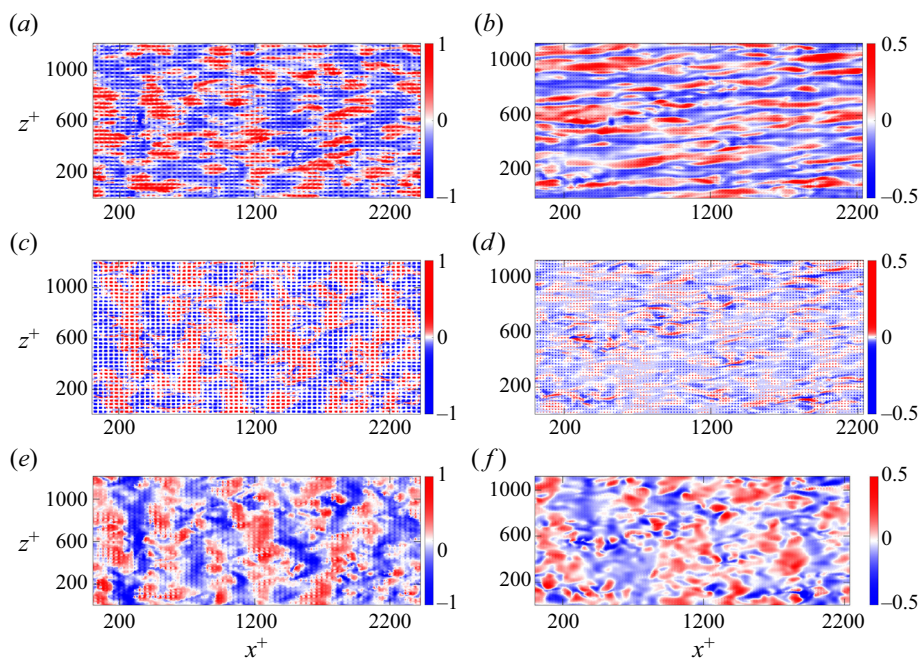
Figure 14. Instantaneous fluctuations of (*a*,*b*) streamwise velocity, (*c*,*d*) wall-normal velocity and (*e*,*f*) pressure at $y^+ = 0$. Here (*a*,*c*,*e*) HP1; (*b*,*d*,*f*) LP1. Flow direction is from left to right. The white regions represent the solid rods of the substrate.

The spectral energy densities at the surface level in figure 15 reveal the signature of the K–H-like structures (indicated with the red lines) observed in figure 12 for HP1. For LP1, no such signature is visible and overall far less flow activity occurs at the permeable surface. Additionally, the spectra show energetic regions at wavelengths equal to the horizontal substrate spacings s_x^+ and s_z^+ (indicated using the green lines) along with their subharmonic wavelengths. These regions represent the pore-coherent flow which is modulated by the ambient turbulence, as similarly occurs over rough surfaces (Abderrahaman-Elena *et al.* 2019). The pore-coherent flow component forming along the spanwise direction repeats periodically along the streamwise direction in intervals of $\lambda_x^+ = s_x^+$. This flow component is modulated by the ambient turbulence and becomes amplified over a broad range of spanwise wavelengths as can be seen in figure 15(*a*,*b*) for the *u* and *v* spectra of HP1. A similar effect takes place for the pore-coherent flow component forming along the streamwise direction. While the pore-coherent flow does exist for LP1, it is significantly weaker compared with HP1. Regarding the HP2′ and HP3′ cases, some delicate differences can be observed compared with HP2 and HP3, but the assessment of them is not done here and is instead gathered in Appendix C for the interested reader.

Ultimately, the modulated pore-coherent flow (areas enclosed by green lines in the spectra of figure 15) and its subharmonics for the HP cases are seemingly attributable to the energetically coherent ambient turbulent scales, particularly those associated with the K–H-like structures. This would explain why the LP cases, despite having streamwise and spanwise pitches of comparable size to those of the HP cases, do not exhibit similarly strong pore-coherent flows. Broadband excitation of any flow component induced by the geometry of the porous substrate is contingent upon the existence of broadband
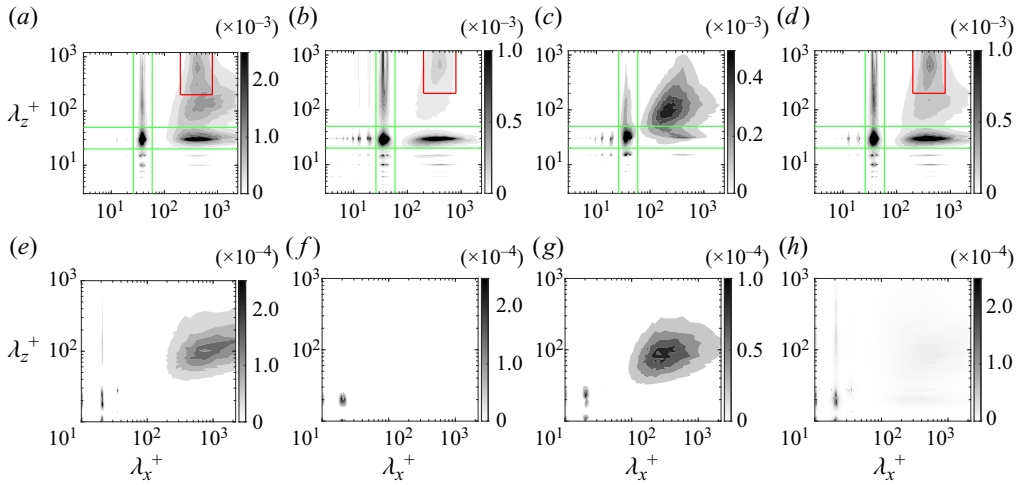
Figure 15. Premultiplied two-dimensional spectral densities: (a,e) $k_x k_z E_{uu}$; (b,f) $k_x k_z E_{vv}$; (c,g) $k_x k_z E_{ww}$; (d,h) $k_x k_z E_{uv}$ at $y^+ = 0$. Here $(a–d)$ HP1; $(e–h)$ LP1. The red lines demarcate $200 \lesssim \lambda_x^+ \lesssim 800$ and $200 \lesssim \lambda_z^+$. The green lines enclose the signature of the pore-coherent flow which are coincident with $\lambda_x^+ = s_x^+$ and $\lambda_z^+ = s_z^+$.

energetic turbulent scales. The observations made here have important implications for the subsurface flow since the pore-coherent flow, which undergoes modulation by the ambient turbulence, factors into the scale-selection that takes place at the surface and therefore the scales of motion that occur inside the substrates.

5. Subsurface flow

Thus far, the effects due to the presence of a porous substrate have been examined for the overlying flow. Attention is now given to the subsurface flow that develops inside the substrates.

5.1. *Mean flow, fluctuating velocities and Reynolds shear stress*

First, the mean velocity along with the fluctuations of the different velocity components are examined. Figure 16 demonstrates that the mean flow develops a region of negative shear beneath the surface. This negative shear is induced by the overlying K–H-like structures (Endrikat *et al.* 2021). As such, it is notable for the HP cases, while a very weak mean flow develops inside the substrates for the LP cases. Within the region of negative shear, the mean flow undergoes flow reversal. Larger wall-normal pore spacings cause this region to become extended and the position at which the flow undergoes reversal corresponds to the bottom of the first pore layer, i.e. $y^+ \approx -s_y^+$. The exponential decay exhibits similarity across the different HP cases, but requires both a large enough wall-normal pore spacing and K–H-like flow to develop at the surface since the LP cases do not exhibit such a quality.

The Reynolds shear stress undergoes a sign reversal for the HP cases which the LP cases do not (figure 17). As the first pore layer becomes deeper, this reversal region becomes extended. Overall, however, $-\overline{u'v'}^+$ is weak below the surface. Cases HP2′ and HP3′ exhibit the same pattern as the other HP cases.

For the velocity fluctuations (figure 18), all of them gradually decay towards the floor of the porous substrates where they become forcibly dampened due to the no-slip condition.
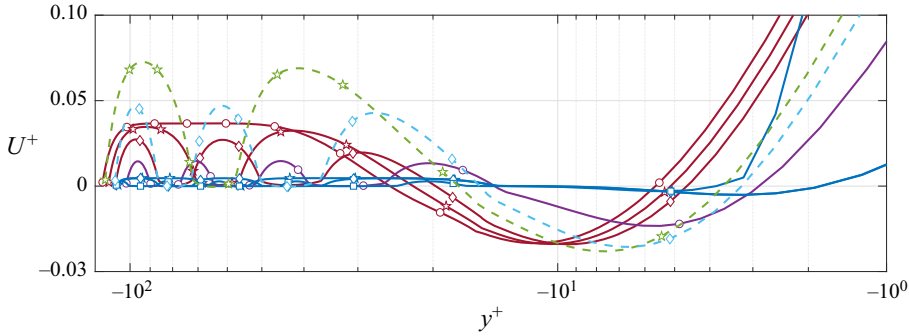
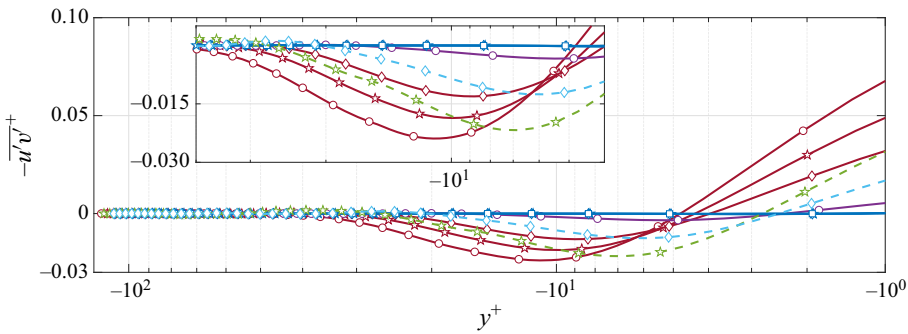Figure 16. Mean velocity profiles inside the substrates for the cases of table 1.

Figure 17. Reynolds shear stress profiles inside the substrates for the cases of table 1.

However, both u' and w' undergo dampening at the bottom of each pore layer as evident by their oscillatory patterns, whereas v' largely demonstrates a monotonic decay. Considering the downward path from a surface pore-opening; the wall-normal flow entering an opening will not come across any barriers along the way towards the substrate floor since it moves through what is essentially a narrow duct. For wall-parallel flow, however, at the bottom of each pore layer the interconnected rods of the substrate's geometry will impede any in-plane motion. The overall magnitude of the spanwise velocity fluctuations is less than those of the streamwise and wall-normal velocity fluctuations, which follows from the spanwise velocity also being the least energetic velocity component at the surface of the substrates. Note that the magnitude of v' entering the substrate remains the same as it is above-surface, while the magnitudes of both u' and w' become strongly diminished. This relates to what was said earlier about v' facing less impediment as it moves through the substrate. The dense layer of solid at the substrate top strongly impedes wall-parallel motion as it penetrates into the substrate compared with wall-normal motion. Here HP2′ and HP3′ have stronger streamwise fluctuations compared with HP2 and HP3. This can primarily be attributed to their larger K_x^+, resulting in less impedance of streamwise momentum, but may also be attributable to the stronger turbulence at the surface (figures 6 and 11), resulting in a greater modulation of the subsurface flow, an aspect which will be examined in § 6.

Some of the observations made here have been similarly reported for turbulent flows over engineered dense canopies (Sharma & García-Mayoral 2020), such as the gradual decay of the wall-normal fluctuations. Periodic dampening of the fluctuations were not reported for the canopy flows, but this is attributable to the porous substrates having layers
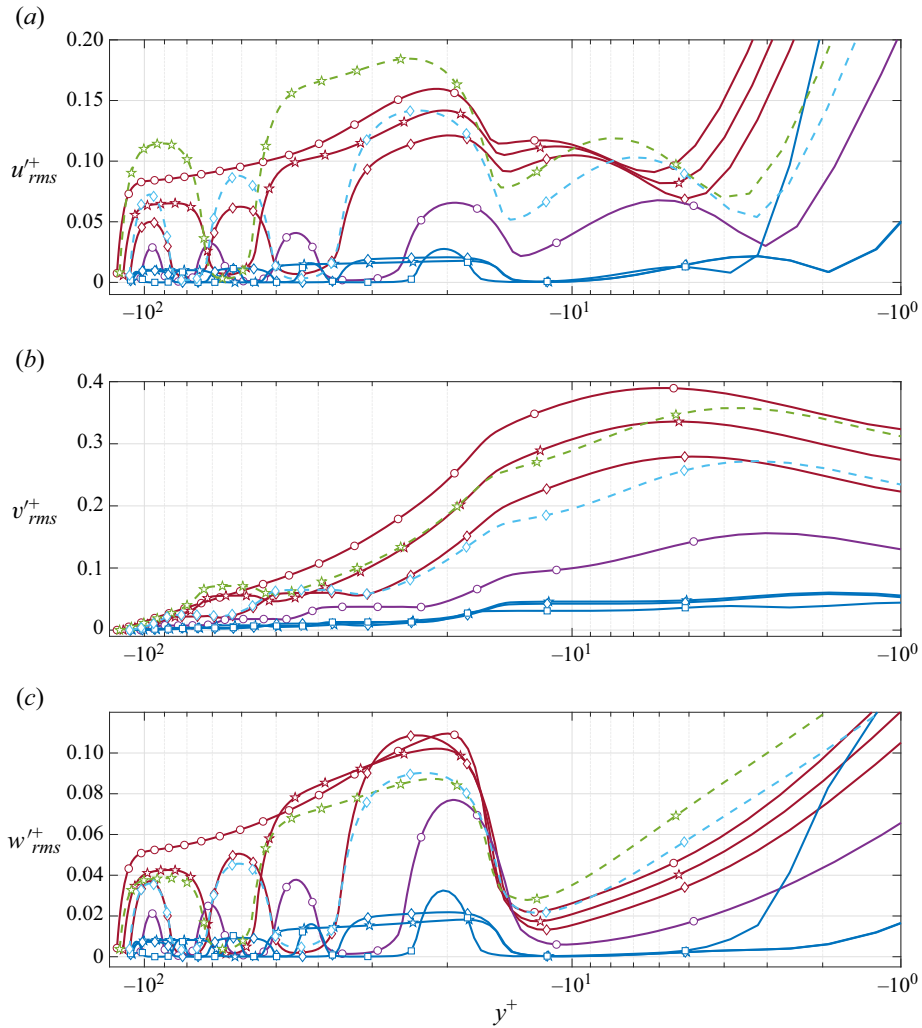
Figure 18. Streamwise (*a*), wall-normal (*b*) and spanwise (*c*) r.m.s. velocity fluctuations within the porous substrates.

of interconnected solid elements whereas canopy posts are isolated from one another and do not place similar restrictions on in-plane fluid motion. Similar dampening patterns were observed in the DNS of Kuwata & Suga (2017) and the experiments of Suga, Okazaki & Kuwata (2020).

5.2. *Flow structure and features*

The surface flow was described in § 4 and bearing in mind the observations made there the subsurface flow is now examined by assessing the instantaneous fluctuations within the first pore layer at $y^+ \approx -15$ in figure 19. The flow fields of both HP2 and HP3 show spanwise elongated patterns in both their streamwise and wall-normal velocity fluctuations (figure 19*a,e,b,f*). The pressure fluctuations of both HP2 (figure 19*i*) and HP3 (figure 19*j*) reflect the patterns of their streamwise and wall-normal velocity fluctuations. Kuwata & Suga (2016) attributed the velocity fluctuations occurring within the porous substrate to
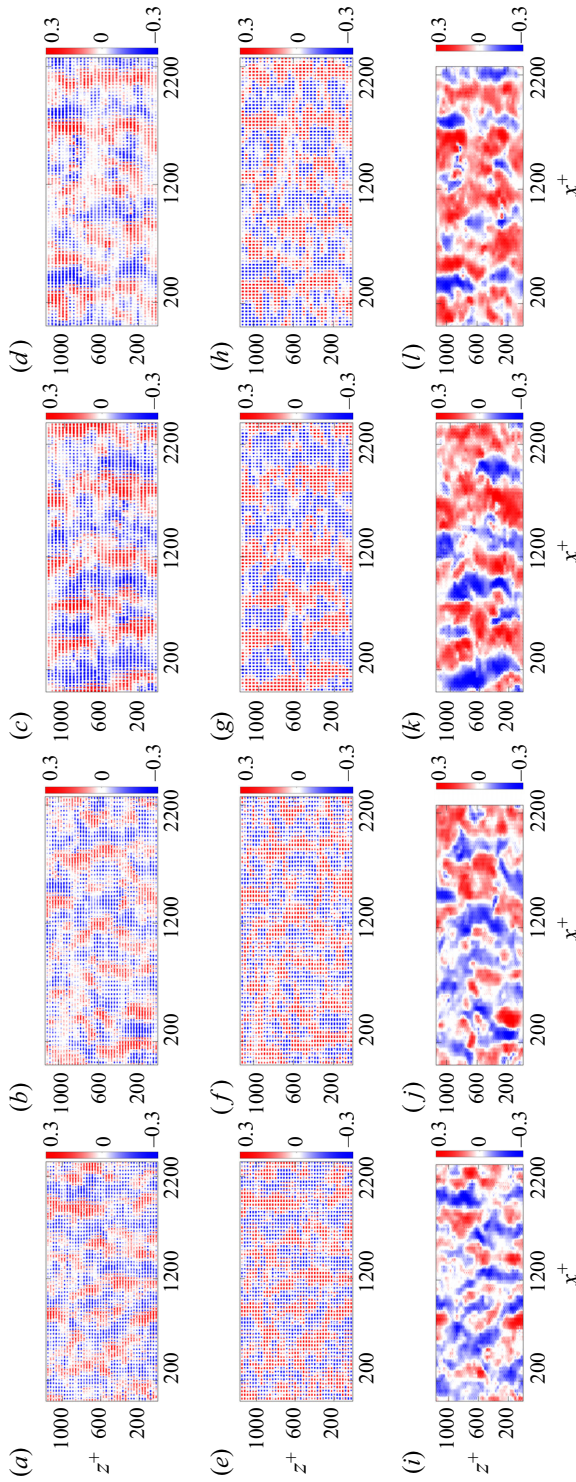
Figure 19. Instantaneous fluctuations of (*a–d*) streamwise velocity, (*e–h*) wall-normal velocity and (*i–l*) pressure at $y^+ \approx -15$: (*a,e,i*) HP2; (*b,f,j*) HP3; (*c,g,k*) HP2′; (*d,h,l*) HP3′. Flow direction is from left to right. The white regions are due to the presence of the porous substrate's rods.
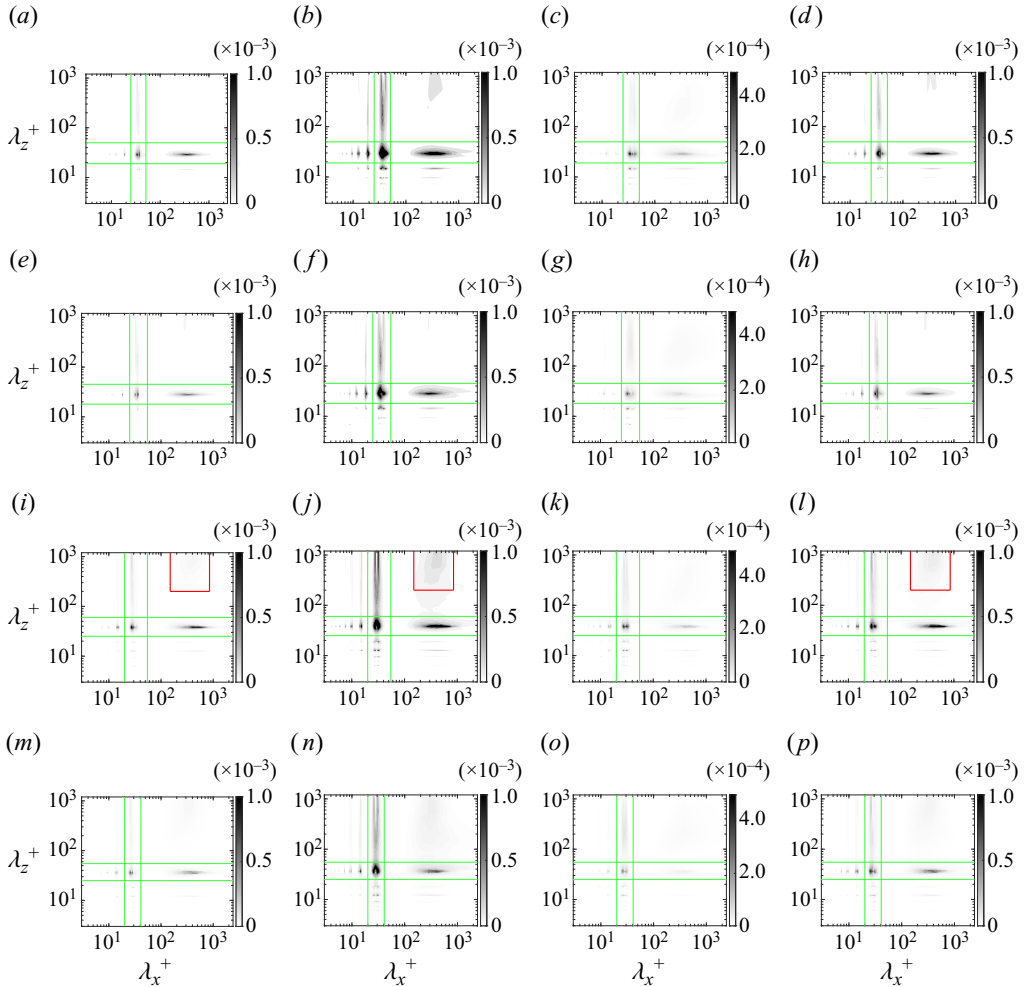
Figure 20. Premultiplied spectral densities: (a,e,i,m) $k_x k_z E_{uu}$; (b,f,j,n) $k_x k_z E_{vv}$; (c,g,k,o) $k_x k_z E_{ww}$; (d,h,l,p) $k_x k_z E_{uv}$ at $y^+ \approx -15$. Here $(a–d)$ HP2; $(e–h)$ HP3; $(i–l)$ HP2$'$; $(m–p)$ HP3$'$. Note the differences in the overall magnitude of the contours for the different cases. The green lines enclose the most energetically significant parts of the pore-coherent flow and the red lines those of the K–H-like rollers.

the pressure fluctuations caused by the K–H-like flow at the surface. The observations made here seem to agree with this, as the turbulence in the near-surface region of both HP2 and HP3 falls into the K–H-like regime. The flow field of HP3$'$ (figure 19d,h,l) is similar to HP3 (figure 19b,f,j) with no discernible differences existing between them. The flow field of HP2$'$ in figure 19(c,g,k) shows a stronger spanwise coherency than HP2 in figure 19(a,e,i) (this greater coherency can also be observed in the flow field at $y^+ = 0$ in figure 32, and is attributed to the stronger K–H-like scales visible in the spectra of figure 33).

More details are revealed by examining the spectra of the fluctuations within the first pore layer at $y^+ = -15$, shown in figure 20. The spectra of HP2 and HP3 (figures 20$a–d$ and 20$e–h$) show that almost no ambient turbulence scales penetrate into the substrate. Only the pore-coherent flow remains energetically discernible, as seen by its spectral

signature enclosed by the green lines of figure 20. The pore-coherent flow is also diminished compared with the surface region (figure 33), but not as strongly as the ambient turbulence.

For HP2′, its stronger K–H-like scales at the surface level lead to the survival of those scales down to this depth within the substrate (the regions enclosed by the red lines in figure 20*i,j,l*), although they are quite weak. Despite having the same wall-normal permeability as HP2, the streamwise favourable anisotropy of HP2′ leads to stronger turbulent scales at the surface which are then able to penetrate deeper into the substrate.

Owing to the fact that turbulence does not survive this deep into the porous substrates for HP2, HP3, HP2′ and HP3′, the coherent patterns observed in their flow fields (figure 19) must be attributed to the pore-coherent flow which remains detectable at this depth. The broadband spanwise intensification of the pore-coherent flow, however, is imparted to it from the surface level turbulence which possess spanwise coherent energetic scales. The modulation persists throughout the substrate and hence why the spectra in figure 20 show long patches of spanwise energetic scales, particularly for the wall-normal velocity.

Ultimately, for the porous substrates under consideration here, there exists a notable pore-coherent flow component below the surface, and in some cases weak scales of ambient turbulence related to the K–H-like instability. Similarly, in flows over canopies the fluctuations below the canopy tip-plane are attributed to the strong overlying cross-flow rollers that develop due to the existence of a perturbed mixing layer (Sharma & García-Mayoral 2020). As mentioned previously in § 3.5, for a mixing layer to emerge over porous media, very high effective surface permeability (or permeability Reynolds number) is required (Jiménez *et al.* 2001; Manes *et al.* 2011). Outside of this mixing layer regime, the notable flow activity below the surface mainly resides in the pore-coherent scales of the flow which undergo modulation by the turbulence at substrate's surface. Manes *et al.* (2011) examined whether the resulting eddy structures over their porous foams shared the same characteristics as those reported over canopies and which are associated with an inflectional instability of the mean velocity (White & Nepf 2007). They observed this to not be the case for low to intermediate ranges of permeability. This also applies to the porous substrates examined in this paper and the analysis done to quantify this is gathered in Appendix B.

Before proceeding further, as a final examination to see whether the flow structure inside the substrates undergoes any notable change deeper inside the substrate, the instantaneous fluctuations as well as the spectra at $y^+ \approx -55$ for case HP1 alone are shown in figure 21. One can witness that the patterns are overall similar to those observed at $y^+ \approx -15$ for the rest of the HP cases, with the most notable scales of motion again being those of the pore-coherent flow, while a weak footprint of the K–H-like scales are also present. The existence of the latter at this depth is of course attributable to the stronger overlying K–H-like structures of HP1. In addition, HP1 also lacks interconnected rod layers inside the substrate which would impede downward directed flow. The explanation for the spanwise coherence of the flow field is similar to what was previously described for the flow at the shallower depth of $y^+ \approx -15$. The spectral signature of the pore-coherent flow which encompasses a range of streamwise scales is repeated along the spanwise direction at intervals equal to the spanwise spacing ($\lambda_z^+ = s_z^+$), i.e. between two consecutive pores along this direction. In essence, the patches are collections of narrow fingers of streamwise velocity which are confined to the pores due to a microchannelization effect. These flow elements appear as a spanwise coherent region macroscopically due to being modulated in amplitude, which is what will be examined next.
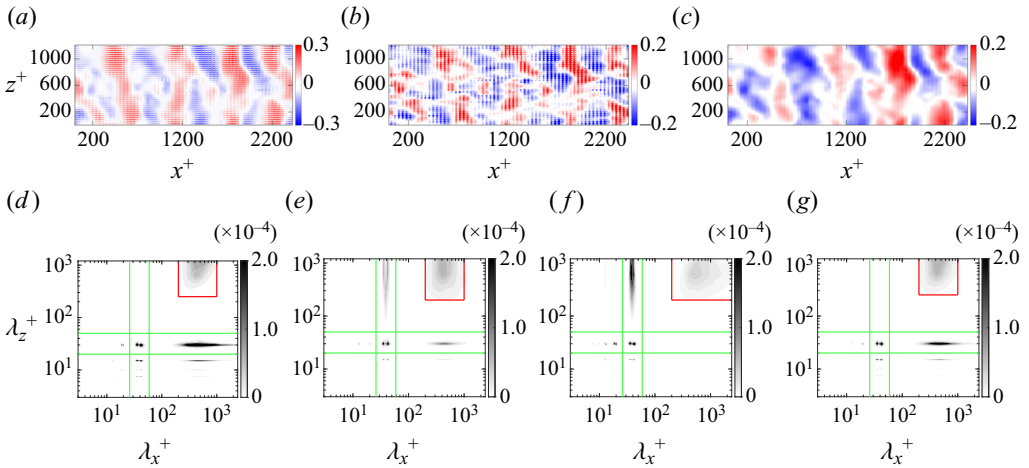
Figure 21. Instantaneous velocity fluctuations and premultiplied spectral energy densities of case HP1 at $y^+ \approx -55$: (*a*) streamwise fluctuations, (*b*) wall-normal fluctuations, (*c*) pressure fluctuations; (*d*) $k_x k_z E_{uu}$, (*e*) $k_x k_z E_{vv}$, (*f*) $k_x k_z E_{ww}$ and (*g*) $k_x k_z E_{uv}$. The green lines enclose the most energetically significant parts of the pore-coherent flow and the red lines the surviving turbulence belonging to the K–H-like scales.
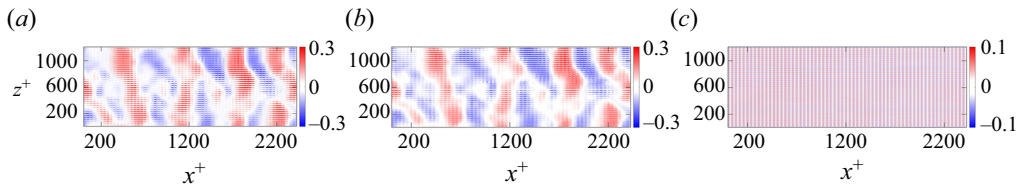

Figure 22. Decomposition of fluctuating streamwise velocity of case HP1 at $y^+ \approx -55$ according to (2.2) and (2.3): (*a*) u'; (*b*) u''; (*c*) $\tilde{u}$.

6. Surface-flow induced AM of subsurface flow

The pore-coherent flow is subject to AM by the scales of the overlying ambient turbulence, evidence of which was provided in the experimental investigation of Kim *et al.* (2020). This phenomenon will now be examined for the substrates considered in this study.

The presence of a solid structure introduces spatial inhomogeneities to the flow field. This gives rise to a dispersive velocity field, $\tilde{u}$, as defined in (2.3). Amplitude modulation, however, is a dynamic effect that is not reflected in the time-averaged dispersive velocity field. The fluctuating velocity along with its different components from (2.2) and (2.3) are shown in figure 22 for case HP1. The dispersive velocity field is weak and does not have irregularities, but as is evident in the spectra of figure 21(*d*), the pore-coherent flow which resides in u'' has a different spatial pattern.

Abderrahaman-Elena *et al.* (2019) conducted a Fourier analysis of the flow within the roughness sublayer of rough-wall turbulence and proposed an algebraic model for decomposing the velocity signals into its background and roughness-coherent (the rough-wall analogue of the pore-flow) components. Their decomposition accounts for the cross-interaction of the velocities across the different flow components and the modulations that arise as a result of them. As such, the model can be used to decompose the velocities even in the event that some degree of scale overlap between the background and roughness-coherent flow exists. When scale-separation between the two flow components
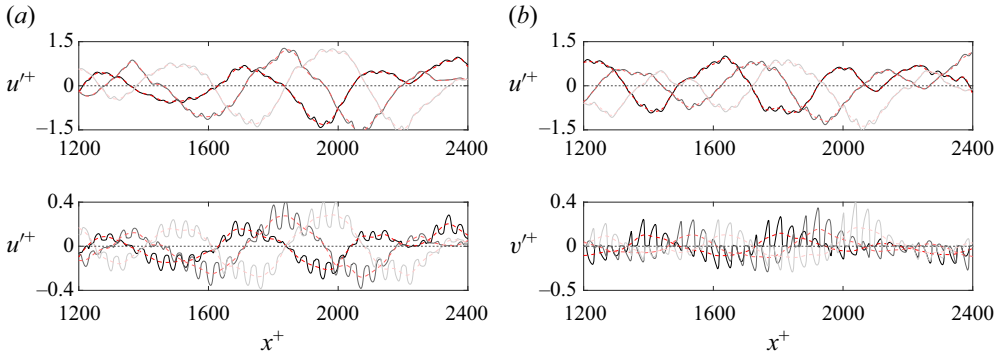
Figure 23. Raw (——) and low-pass filtered (− −, red) spanwise-averaged velocity signals of case HP1: (*a*) streamwise velocity fluctuations at both $y^+ \approx 5$ and $y^+ = 0$, (*b*) streamwise velocity fluctuations at $y^+ \approx 5$ and wall-normal velocity fluctuations at $y^+ = 0$. The solid to faded lines represent three successive time signals.

exist, the model functions similar to regular Fourier filtering. Since for the porous substrates examined here the wavelengths of the pore-coherent flow and those of the ambient turbulence do not significantly overlap, regular Fourier filtering has been employed to separate the flow components and quantify AM. This is demonstrated in figure 23, where the high-frequency (low-wavelength) amplitude-modulated signal of the pore-coherent flow has been removed from the streamwise velocity signal at the surface ($y^+ = 0$) using low-pass filtering. This recovers the low-frequency (long-wavelength) signal of the ambient turbulence. There does not seem to be a discernible AM effect above the surface at $y^+ \approx 5$, as the pore-flow component (the undulations of the black line) does not undergo notable changes in amplitude. The AM effect is similarly demonstrated for the wall-normal velocity in figure 23. Note that this AM phenomenon is different from AM observed in canonical turbulent flows between the inner and outer flow regions (Mathis, Hutchins & Marusic 2009). That effect is due to the existence of large-scale structures within the log-layer which emerge when the Reynolds number becomes sufficiently large ($Re_\tau > 1700$).

The approach undertaken here to quantify AM follows that of Mathis *et al.* (2009), where the correlation between the low-pass filtered (large-scale) streamwise velocity fluctuations, u'_L, and the long-wavelength envelope of the high-pass filtered (small-scale) velocity fluctuations, $E_L(\boldsymbol{u'_s})$, taken at two different fixed y positions (y_1 for the u'_L and y_2 for u'_s) quantifies the degree of AM (note that $\boldsymbol{u'_s}$ can be any of the velocity components)

$$R_{\boldsymbol{u}}(y_1, y_2) = \frac{\overline{u'_L \, E_L(\boldsymbol{u'_s})}}{\sqrt{\overline{u'^2_L}}\sqrt{\overline{E_L(\boldsymbol{u'_s})^2}}}. \tag{6.1}$$

In (6.1), E denotes the envelope of a signal and is acquired using the Hilbert transform. The Hilbert transform of a real-valued function, $f(t)$, produces another real-valued function, $\tilde{f}(t)$. Together, $f(t)$ and $\tilde{f}(t)$ form a harmonic conjugate pair and define the complex analytic signal of $f(t)$,

$$F(t) = f(t) + i\tilde{f}(t) = E(t)e^{i\phi(t)}. \tag{6.2}$$

This provides the instantaneous envelope, $E(t)$, and phase, $\phi(t)$, allowing for the demodulation of the original modulated signal, $f(t)$. More details regarding the Hilbert transform may be found in Mathis *et al.* (2009) and the references contained therein.
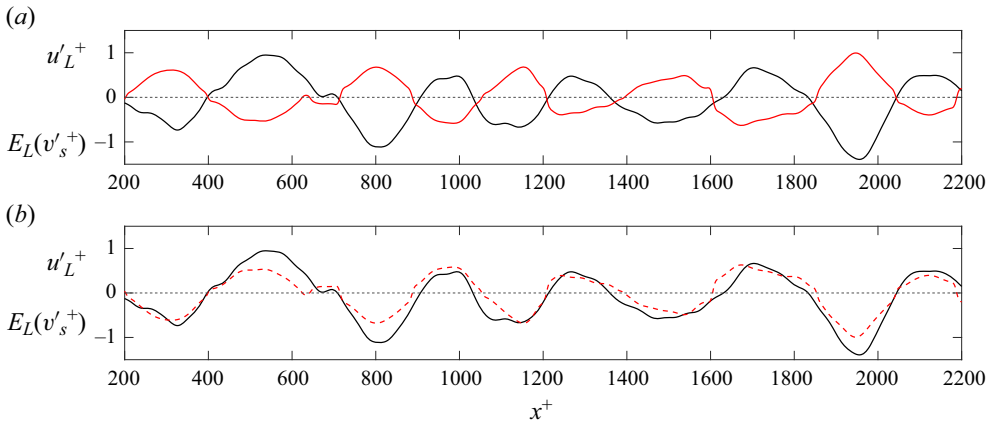
Figure 24. Amplitude modulation of v by u. Panel (a) shows large-scale streamwise velocity fluctuations (——) at $y^+ \approx +5$ and the long-wavelength envelope of small-scale wall-normal velocity fluctuations (——, red) at $y^+ = 0$ of case HP2; panel (b) shows the same, only with the envelope ($--$, red) now phase-shifted by π.

Other approaches can also be used to the assess modulation effects, such as wavelet analysis used by Baars *et al.* (2015) to quantify AM and frequency modulation effects. The Hilbert-based approach, however, remains robust. The long-wavelength envelope of small-scale velocity, $E_L(\boldsymbol{u'_s})$, obtained after taking the Hilbert transform of the velocity time-signal, is then high-pass filtered to keep only the modulated small-scale velocity signal. Unlike in experimental measurements, the velocity signals here are not single-point measurements. Instead, spanwise-averaged one-dimensional velocity signals at different y^+ planes are used to first obtain instantaneous correlations and then followed by ensemble-averaging over all temporal samples to obtain a single correlation coefficient.

Figure 24(a) shows how the small-scale wall-normal velocity fluctuations at the permeable surface are modulated in amplitude by the large-scale streamwise velocity fluctuations of the ambient turbulence above it. The envelope of v'_s rises and falls along with the variations in the amplitude of u'_L. The high degree of correlation becomes clearer when considering figure 24(b), where the envelope of v'_s is phase-shifted by π, making it overlap to a significant extent with the signal of u'_L. This also demonstrates that events of u and v are almost always in antiphase with respect to one another close to the surface. Such a modulation effect is not observed between u'_L and w'_s in figure 25. This does not, however, mean that a modulation of w does not take place, as all three velocity components cross-interact with and modulate one another (Abderrahaman-Elena *et al.* 2019). It only suggests that a modulating effect exclusively directed from u to w does not seem to be occurring in this instance.

The instantaneous frequencies of the velocities can be calculated from their analytic signals obtained using the Hilbert transform. These can then be used to calculate the instantaneous phase-difference between the streamwise and wall-normal velocities. A probability density histogram of instantaneous phase differences is shown in figure 26(b) for case HP1, demonstrating that u' and v' are predominately in antiphase. The probability density histogram for the AM correlation coefficient (6.1) is shown in figure 26(a) and demonstrates the persistent presence of AM between the u' and v' as they evolve in time while the same is not observed between u' and w' in figure 26(d,c).

Examination of the flow inside the substrates (figures 21 and 22) demonstrated that AM is present within them. As such, it is of interest to see how deep the effect persists and
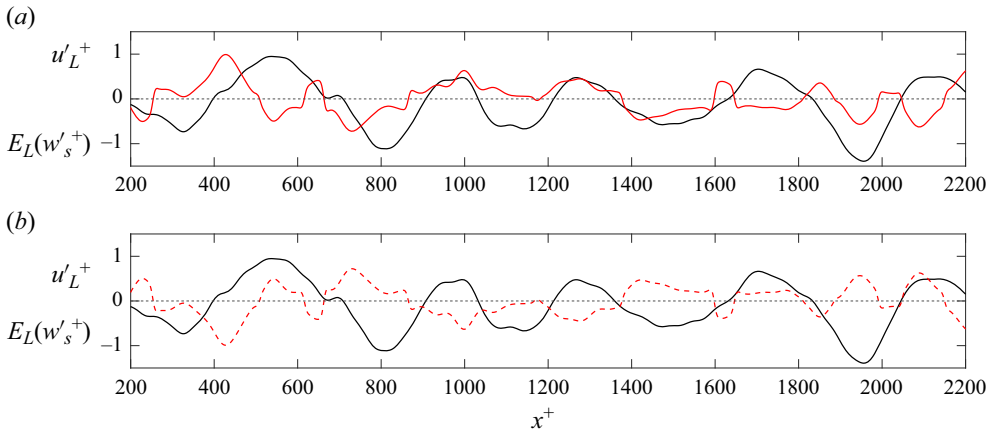
Figure 25. Lack of AM of w by u. The plots are similar to those in figure 24, but with the envelope of the spanwise velocity instead of the wall-normal velocity.
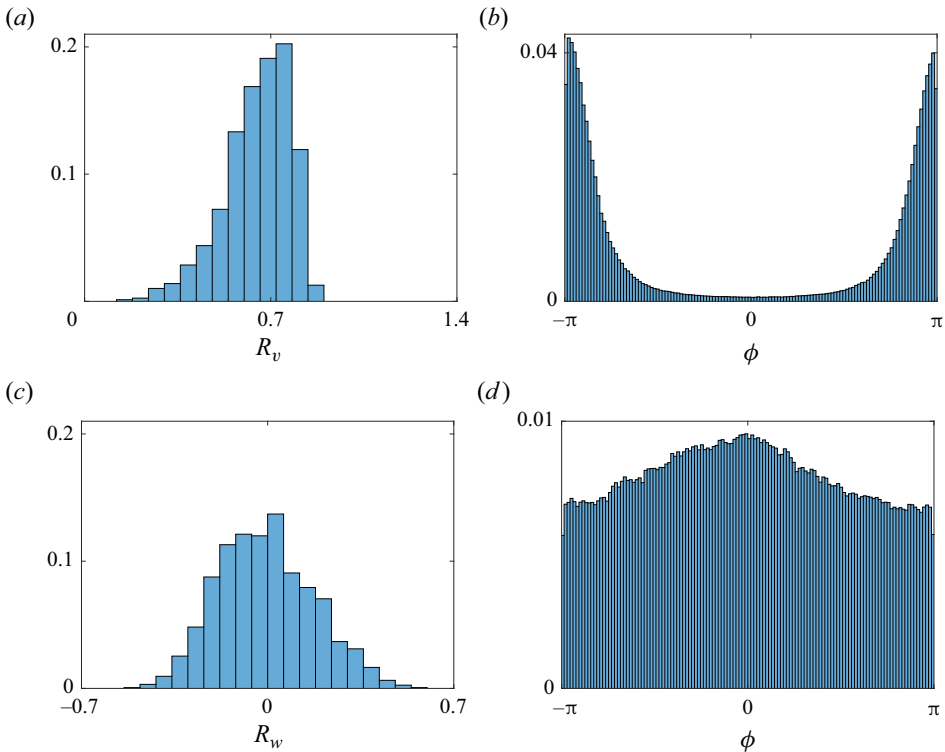

Figure 26. Probability density histograms of AM correlation between (*a*) $u'_L{}^+$ and $E_L(v'_s{}^+)$, and (*c*) $u'_L{}^+$ and $E_L(w'_s{}^+)$. Instantaneous phase differences between (*b*) $u'_L{}^+$ and $v'_L{}^+$, (*d*) $u'_L{}^+$ and $w'_L{}^+$ for case HP2. The u' signal was taken at $y^+ \approx 5$ while the v' and w' were taken at $y^+ = 0$.

also how its strength differs between the various substrates. Figure 27 displays the AM effect on the wall-normal velocity at different depths for the substrates of table 1. The AM remains quite strong halfway down into the substrates for the HP cases. It is much weaker
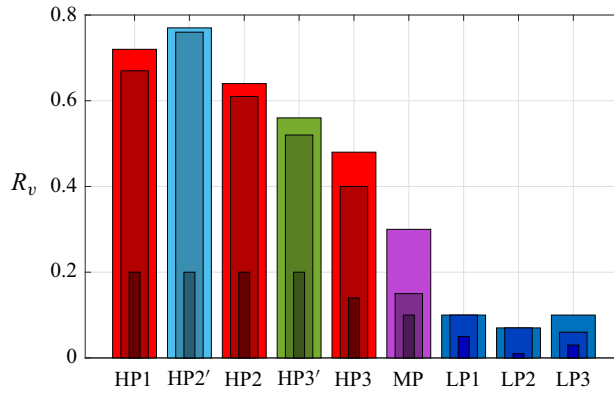
Figure 27. Degree of AM of the wall-normal velocity. Light to darker shades correspond to $y^+ \approx -5$, $y^+ \approx -50$ and $y^+ \approx -110$, respectively.

overall for the LP cases, highlighting how the energetic surface level dynamics of the HP cases which fall into the K–H-like regime enhances this effect.

7. Summary and conclusions

Direct numerical simulations of turbulent flows in an open channel geometry where the wall-side of the channel is covered by a porous substrate have been carried out in this work. Anisotropic porous substrates with permeability components of different values were first assessed in how they cause changes in the overlying turbulent flow. When the wall-impedance condition becomes weakened, near-wall turbulence undergoes a transition away from its canonical structure – characterized by the presence of streaks and quasistreamwise vortices – to one where spanwise coherent structures reminiscent of the K–H instability emerge.

The primary permeability component of significance in determining wall-impedance is K_y. An analysis using the K_{Br} permeability criteria of Sharma *et al.* (2017) and Gómez-de Segura *et al.* (2018) for predicting when turbulence transitions to a K–H-like regime remains robust for the DNS data in this study. The K_{Br} condition was obtained using linear stability analysis of permeable wall boundary conditions derived using the Darcy–Brinkman equation but remain applicable to the pore-scale resolved DNS data in this study, indicating that the microstructure details of the porous substrates do not have a leading-order impact on the instability. This agrees with the argument made by White & Nepf (2007), who assessed that only the overall resistance of the porous layer is important and not the details of its geometry in bringing about and sustaining the instability.

Past results in the literature using continuum-based approaches of representing a porous region or using permeable wall boundary conditions have suggested that a reduction in drag is perhaps attainable for certain combinations of permeability, particularly for streamwise preferential anisotropy (Gómez-de Segura & García-Mayoral 2019). However, none of the porous substrates examined here resulted in drag reduction (figure 5*a*). Drag reduction in a passive manner can be obtained if a surface can simultaneously weaken viscous dissipation while impeding turbulent mixing from taking place close to its vicinity, an effect which is quantified in the 'virtual-origin' framework (Luchini 1996; Ibrahim *et al.* 2021). The weakening of viscous dissipation is typically quantified in terms of a slip velocity, which is negligible for the porous substrates tested in this study.
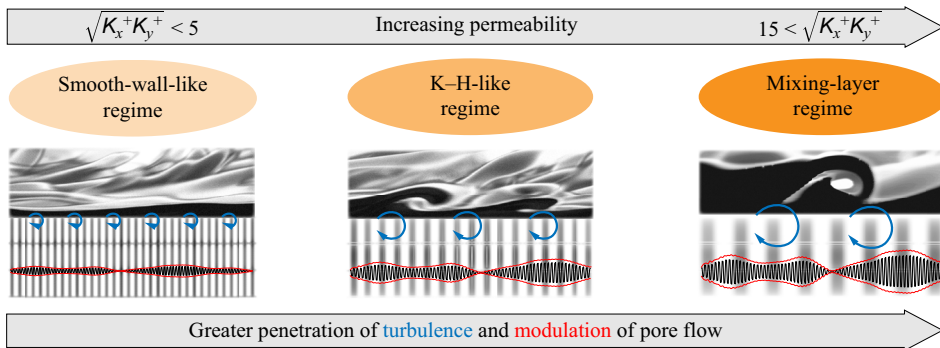
Figure 28. Conceptual sketch showing the evolution of turbulence over porous substrates. The lower limit $\sqrt{K_x^+ K_y^+} < 5$ is based on (3.8) and the threshold shown in figure 9(*d*). The upper limit $15 < \sqrt{K_x^+ K_y^+}$ is inferred from the results of Manes *et al.* (2011) in conjunction with (3.8).

Turbulent activity, however, increases in the vicinity of the surface such that the net effect becomes one of drag increase (figure 7). Streamwise-preferential anisotropy does not lead to a drag reducing effect, which can only occur in the canonical smooth-wall-like regime of near-wall turbulence, and which only the LP cases belong to. They do, however, exhibit a trend of drag decrease with increased streamwise-preferential anisotropy. Ultimately, drag reduction using porous media must be assessed in terms of the slip-velocity (or slip-length) they can cause at the surface.

At the surface of the porous media, spectral analysis reveals the existence of flow signatures conforming to the geometry of the surface and with amplified levels of energy (figure 15). Inside the porous substrates, the surviving turbulence scales become rapidly dampened and the flow component which significant energy-wise is the pore-coherent flow figure 20. The structure of the pore-coherent flow is geometry dependent, which makes the microstructure of the porous medium, particularly at the surface, an important aspect of its design.

The aforementioned pore-coherent flow undergoes significant AM by the ambient turbulent motion present near the surface of the porous media. This AM effect extends deep into the porous media, perturbing its flow and becoming a principal means of inducing flow activity inside it. Stronger ambient turbulence at the surface strengthens this effect, such that it becomes more pronounced for the cases which fall into the K–H-like regime (figure 26). This is because the K–H-like structures lead to greater momentum exchange between the surface and subsurface flow. These flow features are conceptually illustrated in figure 28, where going from left to right indicates an increase in K_y^+ and ultimately K_{Br}^+.

Knowledge of the regimes illustrated in figure 28 and the scale interaction which occurs between the porous media and turbulent flow can be leveraged in applications involving heat and mass transfer. Unlike flow momentum, heat transfer stands to benefit from more intense turbulent activity in the vicinity of the porous medium, as this will lead to greater thermal convection. To what degree this can be exploited, is one example of an interesting line of inquiry that can be pursued in relation to turbulence and porous media.

Author ORCIDs.

- Seyed Morteza Habibi Khorasani https://orcid.org/0000-0001-6520-3261;
- Mitul Luhar https://orcid.org/0000-0002-7970-9762;
- Shervin Bagheri https://orcid.org/0000-0002-8209-1449.

Appendix A. Grid resolution assessment

While the resolution requirements for regular channel flow simulations are well-established throughout the literature (Kim & Moin 1985; Lee & Moser 2015), problems involving fluid–solid interactions need to be assessed on a case-by-case basis. The baseline grid has a resolution of $(N_x, N_y, N_z) = (1620, 324, 810)$. This grid more than suffices for resolving the bulk flow region, but it must be determined whether or not the wall-parallel resolution is sufficient for resolving the solid phase of the porous substrates. With this baseline configuration, the number of wall-parallel grid-points per substrate rod thickness becomes $d/\Delta_{x,z} = 10$. This was chosen based on the grid study results of Sharma & García-Mayoral (2020) which was conducted for turbulent flows over canopies. They showed that such a concentration of points per canopy element was enough to resolve them and their induced flow. Nevertheless, to ensure that this resolution is sufficient, a grid study for case HP1 was carried out using both a coarser and refined grid. The refined grid had a resolution of $(N_x, N_y, N_z) = (3240, 324, 1620)$ giving $d/\Delta_{x,z} = 20$ while the coarser grid of $(N_x, N_y, N_z) = (810, 324, 405)$ gave $d/\Delta_{x,z} = 5$. The wall-normal grid is kept the same, which is stretched in the bulk flow region and achieves a constant spacing at $y \approx 0.0042$ ($y^+ \approx 15$) resulting in $d/\Delta_y = 25$. Case HP1 is chosen since it is has some the strongest flow activity in the substrate region and serves as an appropriate candidate for grid resolution assessment of the HP cases. The LP cases are close to the smooth-wall limit and have very little flow penetrating into the substrate, hence a separate grid resolution assessment for them would be redundant.

From figure 29, it is clear that the baseline grid with $d/\Delta_{x,z} = 10$ resolves the flow in both the bulk and substrate regions well with the results being grid independent at this resolution. For the coarse grid with $d/\Delta_{x,z} = 5$, the discrepancy is highest immediately below the surface for the r.m.s. wall-normal velocity fluctuations where the error is $\approx 7\%$. The sufficiency of the baseline grid resolution is further reinforced by the results in table 3, where the calculated Darcy permeabilities for the porous substrates using the baseline and refined grid resolutions is reported. No appreciable improvement in the permeability estimates was achieved by increasing the number of grid points per rod from $d/\Delta_{x,z} = 10$ to $d/\Delta_{x,z} = 20$.

Appendix B. Assessment of whether or not the K–H-like structures are similar to those of mixing-layer type flows

In the experiments of turbulent flows over porous metal foams conducted by Manes *et al.* (2011), they examined whether the resulting turbulent flow at the permeable surface of the media were similar to those reported by White & Nepf (2007) for sparse porous
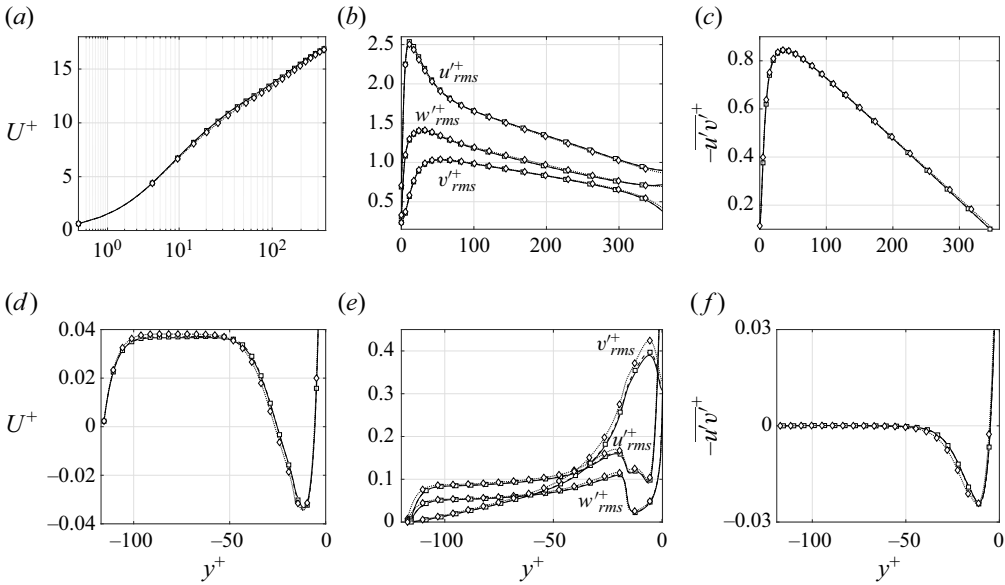
Figure 29. (*a*,*d*) Mean velocity, (*b*,*e*) r.m.s. velocity fluctuations and (*c*,*f*) Reynolds shear stress of the (*a–c*) bulk flow and (*d–f*) substrate regions for HP1. The solid lines represent the results from using $d/\Delta_{x,z} = 20$, the symbols $-\square-$, $d/\Delta_{x,z} = 10$; and $\cdots\lozenge\cdots$, $d/\Delta_{x,z} = 5$.

Case	$\sqrt{K_{x_o}^+}$	$\sqrt{K_{y_o}^+}$	$\sqrt{K_{z_o}^+}$	$\sqrt{K_{x_o}^+}_{HR}$	$\sqrt{K_{y_o}^+}_{HR}$	$\sqrt{K_{z_o}^+}_{HR}$	$\Delta_x\%$	$\Delta_y\%$	$\Delta_z\%$
HP1	3.207	3.437	4.721	3.189	3.417	4.694	−0.56	−0.59	−0.58
HP2	2.738	2.623	3.844	2.723	2.608	3.823	−0.55	−0.58	−0.55
HP3	2.191	2.194	2.805	2.180	2.182	2.791	−0.51	−0.55	−0.50
MP	1.495	1.534	1.495	1.487	1.525	1.487	−0.54	−0.59	−0.54
LP1	1.038	0.734	1.038	1.032	0.729	1.032	−0.58	−0.69	−0.58
LP2	0.912	0.623	0.912	0.907	0.619	0.907	−0.55	−0.65	−0.55
LP3	0.503	0.503	0.503	0.499	0.499	0.499	−0.80	−0.80	−0.80

Table 3. Darcy permeability estimates for the substrates of table 1 using Stokes flow simulations of REVs (such as those shown in figure 3). The permeabilities with the subscript *HR* have a grid resolution of $d/\Delta_{x,z} = 20$ and those without $d/\Delta_{x,z} = 10$. The last three columns list the differences in the permeabilities obtained using the two resolutions.

arrays of cylinders serving as models for vegetation canopies. White & Nepf (2007) demonstrated that the coherent motion at the top of the arrays exhibited a single dominant frequency which was the same as that in free shear layers subject to K–H instability. They therefore characterized the flows as being similar to mixing layers where the instability originates at the inflection point of the mean velocity profile inside the porous region. Manes *et al.* (2011) performed a similar frequency analysis, but observed that only for their highest permeability case did the frequency approach the value associated with mixing-layer type flows. They concluded that for low to moderate permeabilities, the coherent turbulent motion in the vicinity of the permeable surface is not due to the inflectional instability of the mean velocity profile. In a recent DNS study by Wang *et al.* (2022) where transfer entropy was used to measure causal interactions between porous
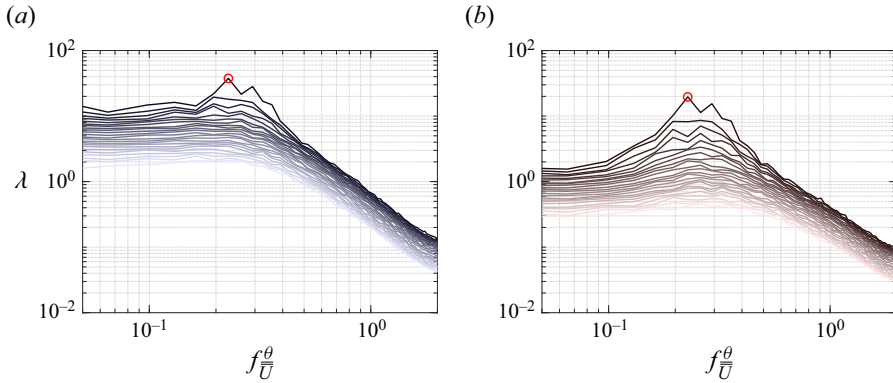
Figure 30. The SPOD eigenvalues of the (*a*) streamwise and (*b*) wall-normal velocity fluctuations at the surface ($y^+ = 0$) of HP1. The peak in the leading SPOD mode at $f = 0.22\bar{U}/\theta$ is circled in red. The shading of the curves varies from dark to bright as the mode number increases.
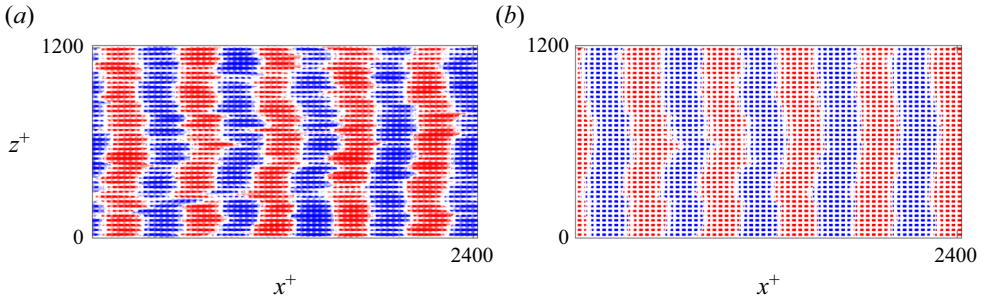

Figure 31. First SPOD mode at $f = 0.22\bar{U}/\theta$ of the (*a*) streamwise and (*b*) wall-normal velocity fluctuations at the surface ($y^+ = 0$) of HP1.

media and turbulent flows, the frequencies at which these interaction took place over the various porous media were in agreement with the results of Manes *et al.* (2011).

The dominant frequency reported by White & Nepf (2007) was $f = 0.032\bar{U}/\theta$, where $\theta = \int_{-\infty}^{\infty}(1/4 + (U - \bar{U}/\Delta U)^2)\,\mathrm{d}y$; $\Delta U = U_{y=\delta} - U_P$; $\bar{U} = (U_{y=\delta} + U_P)/2$ and U_P is the velocity deep inside the porous medium. The frequencies reported by Manes *et al.* (2011) for their porous media ($1.9 \le \sqrt{K^+} \le 8.4$) were much higher than 0.032 and only the case of $\sqrt{K^+} = 17.2$ had a frequency close to $f = 0.032\bar{U}/\theta$.

A similar frequency characterization was performed for HP1 which has the highest wall-normal permeability $\sqrt{K_y^+} = 3.4$ out of all the cases in table 1. First, SPOD (Towne, Schmidt & Colonius 2018) is applied to the surface flow of HP1. Examination of the SPOD eigenvalues in figure 30 reveals a peak in the leading SPOD mode at $f = 0.22\bar{U}/\theta$ for both the streamwise and wall-normal velocity components. This is close to $f \approx 0.22\bar{U}/\theta$ reported by Manes *et al.* (2011) for their metal foam which had a permeability of $\sqrt{K^+} = 3.2$. Observing the first SPOD mode for both the streamwise and wall-normal velocity in figure 31 reveals recurrent spanwise-elongated patterns. Such patterns are not recovered in the SPOD modes for any of the LP cases (not shown). This further demonstrates the regime distinction that was described in §§ 3.4 and 3.5. So it can be concluded that for the porous substrates of table 1, the mixing-layer analogy does not hold, in agreement with the conclusion made by Manes *et al.* (2011).
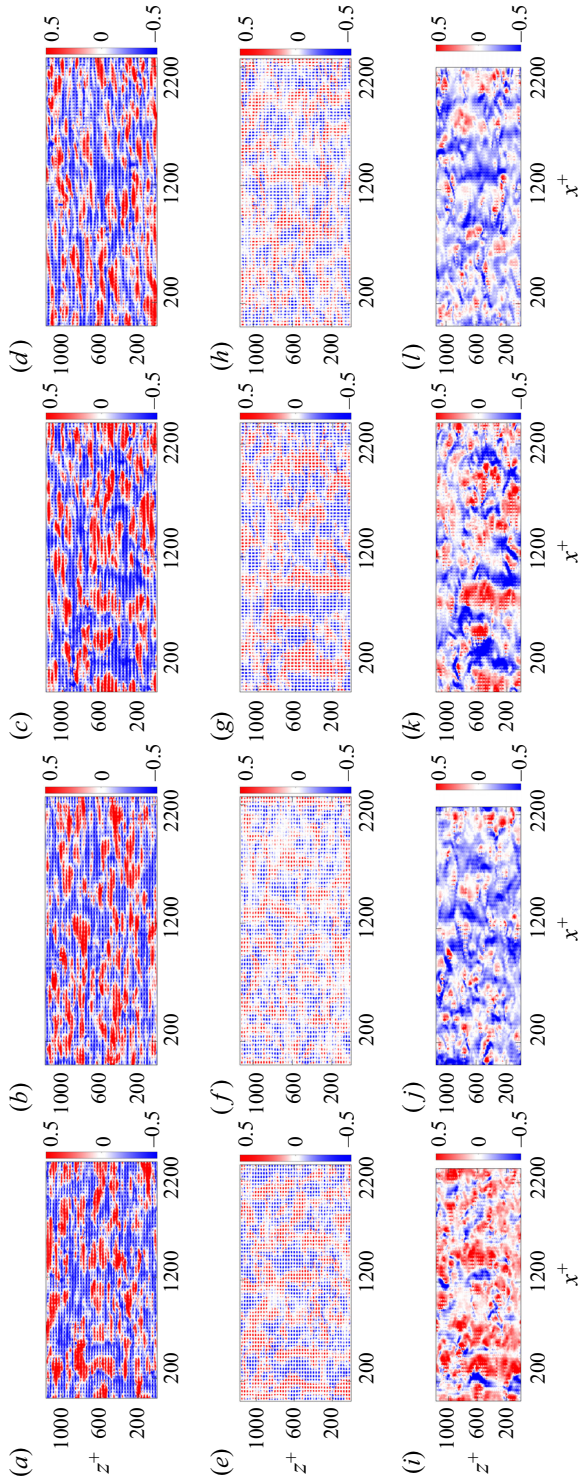
984 A63-34

Figure 32. Instantaneous fluctuations of the (*a–d*) streamwise velocity, (*e–h*) wall-normal velocity and (*i–l*) pressure at $y^+ = 0$: (*a,e,i*) HP2; (*b,f,j*) HP3; (*c,g,k*) HP2′; (*d,h,l*) HP3′. Flow direction is from left to right.
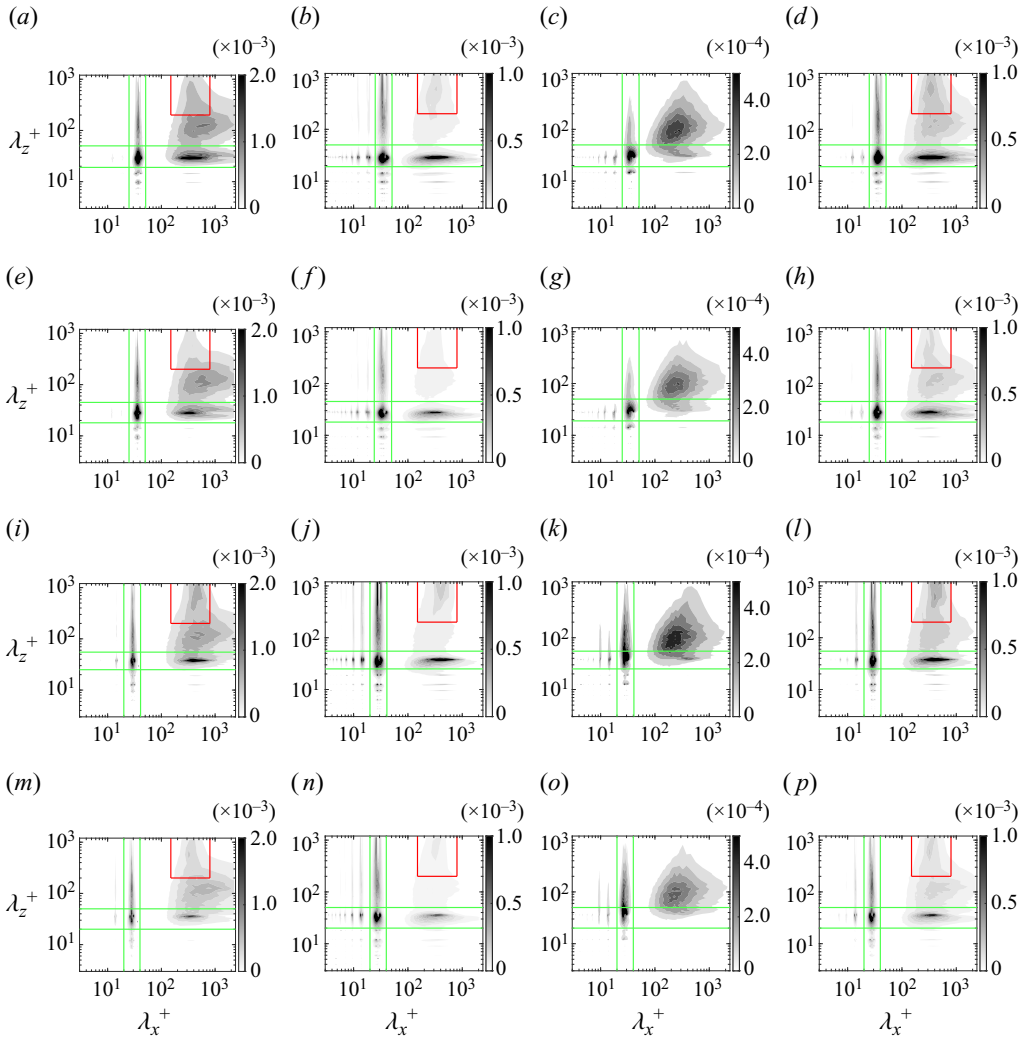
Figure 33. Premuliplied two-dimensional spectral densities: (a,e,i,m) $k_x k_z E_{uu}$; (b,f,j,n) $k_x k_z E_{vv}$; (c,g,k,o) $k_x k_z E_{ww}$; (d,h,l,p) $k_x k_z E_{uv}$ at $y^+ = 0$. Here $(a–d)$ case HP2; $(e–h)$ case HP3; $(i–l)$ case HP2′; $(m–p)$ case HP3′. The green lines enclose the most energetically significant parts of the pore-coherent flow and the red lines those of the K–H-like rollers.

Appendix C. Comparison of surface flow features between HP2, HP3 and HP2′, HP3′

Thus far, it has been shown that the flow structure close to the surface of the substrates are quite different between the LP and HP cases. The LP cases are essentially smooth-wall-like and permit very little turbulent activity from taking place in the proximity of the surface and hence do not motivate further examination. The question now posed is how significant is the pore-coherent flow – determined by wavelengths of the porous medium – relative to the existence of the K–H-like structures. For this purpose, HP2′ and HP3′ are examined. They are similar to HP2 and HP3 but with s_x and s_z exchanged (table 1). The wall-normal permeability in this way remains the same but the pore-coherent flow will change and its

984 A63-36

effect on the flow can be scrutinized. Additionally, the HP2′ and HP3′ have streamwise preferential anisotropy which will be factored into the analysis that follows.

When considering the flow fields of HP2 and HP2′, one can observe a greater degree of spanwise coherence for HP2′ in both its streamwise velocity field (figure 32c) and its wall-normal velocity field (figure 32g) compared with those of HP2 (figure 32a,g). The spatial patterns of the velocity and pressure fields for HP2′ (figure 32c,g,k) also visibly mirror one another, whereas this is less evident for HP2 (figure 32a,e,i).

Examining the spectra in figure 33, it can be observed that the ambient turbulence has broadband spanwise coherent scales, in the range of $200 \lesssim \lambda_x^+ \lesssim 800$ and $200 \lesssim \lambda_z^+$, in both the streamwise velocity (figure 33i,m), wall-normal velocity (figure 33j,n) and Reynolds shear stress (figure 33l,p) spectra of HP2′ and HP3′. The structure of the ambient turbulence in HP2 and HP3 is similar. The spectra of HP2′ do, however, demonstrate a patch of more energetic broadband spanwise scales compared with HP2 (this could be the reason why the flow field of HP2′ in figure 32 manifests a greater degree of spanwise coherency compared with HP2). When examining the pore-coherent flow, which are the areas enclosed by green lines in the spectra of figure 33, the broadband streamwise component of them overlap with the ambient turbulence scales to a certain extent such that a degree of scale interaction is taking place between them, but it is not over a wide enough range of scales to alter the structure of the ambient turbulence. For HP2′ and HP3′, the spanwise pitch length, s_z^+, is larger compared with HP2 and HP3, and thus the streamwise pore-coherent flow component overlaps with the ambient turbulence to a greater extent, but still not great enough to be disruptive to the overall dynamics of the turbulence in the near-surface region.

REFERENCES

ABDERRAHAMAN-ELENA, N., FAIRHALL, C.T. & GARCÍA-MAYORAL, R. 2019 Modulation of near-wall turbulence in the transitionally rough regime. *J. Fluid Mech.* **865**, 1042–1071.

ABDERRAHAMAN-ELENA, N. & GARCÍA-MAYORAL, R. 2017 Analysis of anisotropically permeable surfaces for turbulent drag reduction. *Phys. Rev. Fluids* **2**, 114609.

ANISZEWSKI, W., *et al.* 2021 Parallel, robust, interface simulator (Paris). *Comput. Phys. Commun.* **263**, 107849.

BAARS, W.J., TALLURU, K.M., HUTCHINS, N. & MARUSIC, I. 2015 Wavelet analysis of wall turbulence to study large-scale modulation of small scales. *Exp. Fluids* **56** (10), 1–15.

BREUGEM, W.P. & BOERSMA, B.J. 2005 Direct numerical simulations of turbulent flow over a permeable wall using a direct and a continuum approach. *Phys. Fluids* **17** (2), 025–103.

BREUGEM, W.P., BOERSMA, B.J. & UITTENBOGAARD, R.E. 2006 The influence of wall permeability on turbulent channel flow. *J. Fluid Mech.* **562**, 35–72.

CHEN, Z. & GARCÍA-MAYORAL, R. 2023 Examination of outer-layer similarity in wall turbulence over obstructing surfaces. *J. Fluid Mech.* **973**, A31.

CHUNG, D., HUTCHINS, N., SCHULTZ, M.P. & FLACK, K.A. 2021 Predicting the drag of rough surfaces. *Annu. Rev. Fluid Mech.* **53** (1), 439–471.

CLAUSER, F.H. 1954 Turbulent boundary layers in adverse pressure gradients. *J. Aeronaut. Sci.* **21** (2), 91–108.

COSTA, P. 2018 A FFT-based finite-difference solver for massively-parallel direct numerical simulations of turbulent flows. *Comput. Maths Applics.* **76** (8), 1853–1862.

DARCY, H. 1856 *Les fontaines publiques de la ville de Dijon: exposition et application des principes à suivre et des formules à employer dans les questions de distribution d'eau*, vol. 1. Victor Dalmont.

EFSTATHIOU, C. & LUHAR, M. 2018 Mean turbulence statistics in boundary layers over high-porosity foams. *J. Fluid Mech.* **841**, 351–379.

ENDRIKAT, S., MODESTI, D., GARCÍA-MAYORAL, R., HUTCHINS, N. & CHUNG, D. 2021 Influence of riblet shapes on the occurrence of Kelvin–Helmholtz rollers. *J. Fluid Mech.* **913**, A37.

FINNIGAN, J. 2000 Turbulence in plant canopies. *Annu. Rev. Fluid Mech.* **32** (1), 519–571.

FINNIGAN, J.J., SHAW, R.H. & PATTON, E.G. 2009 Turbulence structure above a vegetation canopy. *J. Fluid Mech.* **637**, 387–424.

GARCÍA-MAYORAL, R., GÓMEZ-DE SEGURA, G. & FAIRHALL, C.T. 2019 The control of near-wall turbulence through surface texturing. *Fluid Dyn. Res.* **51** (1), 011410.

GÓMEZ-DE SEGURA, G. & GARCÍA-MAYORAL, R. 2019 Turbulent drag reduction by anisotropic permeable substrates – analysis and direct numerical simulations. *J. Fluid Mech.* **875**, 124–172.

GÓMEZ-DE SEGURA, G., SHARMA, A. & GARCÍA-MAYORAL, R. 2018 Turbulent drag reduction using anisotropic permeable substrates. *Flow Turbul. Combust.* **100** (4), 995–1014.

HABIBI KHORASANI, S.M., LĀCIS, U., PASCHE, S., ROSTI, M.E. & BAGHERI, S. 2022*b* Near-wall turbulence alteration with the transpiration-resistance model. *J. Fluid Mech.* **942**, A45.

HABIBI KHORASANI, S.M., LUHAR, M. & BAGHERI, S. 2022*a* Turbulent flows over engineered anisotropic porous substrates. arXiv:2210.10140v1.

HAMA, F.R. 1954 Boundary layer characteristics for smooth and rough surfaces. *Trans. Soc. Nav. Archit. Mar. Engrs* **62**, 333–358.

HASSAN, Y.A. & DOMINGUEZ-ONTIVEROS, E.E. 2008 Flow visualization in a pebble bed reactor experiment using PIV and refractive index matching techniques. *Nucl. Engng Des.* **238** (11), 3080–3085.

IBRAHIM, J.I., GÓMEZ-DE-SEGURA, G., CHUNG, D. & GARCÍA-MAYORAL, R. 2021 The smooth-wall-like behaviour of turbulence over drag-altering surfaces: a unifying virtual-origin framework. *J. Fluid Mech.* **915**, A56.

JACKSON, P.S. 1981 On the displacement height in the logarithmic velocity profile. *J. Fluid Mech.* **111**, 15–25.

JIMÉNEZ, J. 1994 On the structure and control of near wall turbulence. *Phys. Fluids* **6** (2), 944–953.

JIMÉNEZ, J., UHLMANN, M., PINELLI, A. & KAWAHARA, G. 2001 Turbulent shear flow over active and passive porous surfaces. *J. Fluid Mech.* **442**, 89–117.

KAZEMIFAR, F., BLOIS, G., AYBAR, M., PEREZ CALLEJA, P., NERENBERG, R., SINHA, S., HARDY, R.J., BEST, J., SAMBROOK SMITH, G.H. & CHRISTENSEN, K.T. 2021 The effect of biofilms on turbulent flow over permeable beds. *Water Resour. Res.* **57** (2), e2019WR026032.

KIM, T., BLOIS, G., BEST, J.L. & CHRISTENSEN, K.T. 2020 Experimental evidence of amplitude modulation in permeable-wall turbulence. *J. Fluid Mech.* **887**, A3.

KIM, J. & MOIN, P. 1985 Application of a fractional-step method to incompressible Navier–Stokes equations. *J. Comput. Phys.* **59** (2), 308–323.

KURUNERU, S.T.W., VAFAI, K., SAURET, E. & GU, Y. 2020 Application of porous metal foam heat exchangers and the implications of particulate fouling for energy-intensive industries. *Chem. Engng Sci.* **228**, 115968.

KUWATA, Y. & SUGA, K. 2016 Lattice Boltzmann direct numerical simulation of interface turbulence over porous and rough walls. *Intl J. Heat Fluid Flow* **61**, 145–157.

KUWATA, Y. & SUGA, K. 2017 Direct numerical simulation of turbulence over anisotropic porous media. *J. Fluid Mech.* **831**, 41–71.

LEE, M. & MOSER, R.D. 2015 Direct numerical simulation of turbulent channel flow up to $Re_\tau \approx 5200$. *J. Fluid Mech.* **774**, 395–415.

LUCHINI, P. 1996 Reducing the turbulent skin friction. In *Computational methods in applied sciences 96 (Paris, 9–13 September 1996)* (ed. J.A. Désidéri, C. Hirsch, P. Le Tallec, E. Oñate, M. Pandolfi, J. Périaux & E. Stein), pp. 465–470. John Wiley & Sons Ltd.

LUCHINI, P. 2015 The relevance of longitudinal and transverse protrusion heights for drag reduction by a superhydrophobic surface. In *Proc. European Drag Reduction and Flow Control Meeting – EDRFMC 2015; March 23–26*, pp. 81–82.

LUCHINI, P. 2018 Structure and interpolation of the turbulent velocity profile in parallel flow. *Eur. J. Mech. (B/Fluids)* **71**, 15–34.

LUCHINI, P. 2024 The open channel in a uniform representation of the turbulent velocity profile across all parallel geometries. *J. Fluid Mech.* **979**, R1.

LUCHINI, P., MANZO, F. & POZZI, A. 1991 Resistance of a grooved surface to parallel flow and cross-flow. *J. Fluid Mech.* **228**, 87–109.

MACDONALD, M., CHAN, L., CHUNG, D., HUTCHINS, N. & OOI, A. 2016 Turbulent flow over transitionally rough surfaces with varying roughness densities. *J. Fluid Mech.* **804**, 130–161.

MACDONALD, M., OOI, A., GARCÍA-MAYORAL, R., HUTCHINS, N. & CHUNG, D. 2018 Direct numerical simulation of high aspect ratio spanwise-aligned bars. *J. Fluid Mech.* **843**, 126–155.

MANES, C., POGGI, D. & RIDOLFI, L. 2011 Turbulent boundary layers over permeable walls: scaling and near-wall structure. *J. Fluid Mech.* **687**, 141–170.

MANES, C., POKRAJAC, D., MCEWAN, I. & NIKORA, V. 2009 Turbulence structure of open channel flows over permeable and impermeable beds: a comparative study. *Phys. Fluids* **21** (12), 125109.

MATHIS, R., HUTCHINS, N. & MARUSIC, I. 2009 Large-scale amplitude modulation of the small-scale structures in turbulent boundary layers. *J. Fluid Mech.* **628**, 311–337.

PARAVENTO, F., POURQUIE, M.J. & BOERSMA, B.J. 2008 An immersed boundary method for complex flow and heat transfer. *Flow Turbul. Combust.* **80** (2), 187–206.

REYNOLDS, O. 1895 IV. On the dynamical theory of incompressible viscous fluids and the determination of the criterion. *Phil. Trans. R. Soc. Lond.* A **186**, 123–164.

REYNOLDS, W.C. & HUSSAIN, A.K.M.F. 1972 The mechanics of an organized wave in turbulent shear flow. Part 3. Theoretical models and comparisons with experiments. *J. Fluid Mech.* **54** (2), 263–288.

ROSTI, M.E., BRANDT, L. & PINELLI, A. 2018 Turbulent channel flow over an anisotropic porous wall – drag increase and reduction. *J. Fluid Mech.* **842**, 381–394.

SHAHZAD, H., HICKEL, S. & MODESTI, D. 2023 Turbulence and added drag over acoustic liners. *J. Fluid Mech.* **965**, A10.

SHARMA, A. & GARCÍA-MAYORAL, R. 2020 Turbulent flows over dense filament canopies. *J. Fluid Mech.* **888**, A2.

SHARMA, A., GOMEZ-DE SEGURA, G. & GARCIA-MAYORAL, R. 2017 Linear stability analysis of turbulent flows over dense filament canopies. In *Tenth International Symposium on Turbulence and Shear Flow Phenomena* (ed. L. Smits & H.M. Nagib). Begel House.

SPALART, P.R. & MCLEAN, J.D. 2011 Drag reduction: enticing turbulence, and then an industry. *Phil. Trans. R. Soc.* A **369** (1940), 1556–1569.

SUGA, K., MORI, M. & KANEDA, M. 2011 Vortex structure of turbulence over permeable walls. *Intl J. Heat Fluid Flow* **32** (3), 586–595.

SUGA, K., OKAZAKI, Y. & KUWATA, Y. 2020 Characteristics of turbulent square duct flows over porous media. *J. Fluid Mech.* **884**, A7.

TOWNE, A., SCHMIDT, O.T. & COLONIUS, T. 2018 Spectral proper orthogonal decomposition and its relationship to dynamic mode decomposition and resolvent analysis. *J. Fluid Mech.* **847**, 821–867.

TOWNSEND, A.A. 1976 *The Structure of Turbulent Shear Flow*, 2nd edn. Cambridge University Press.

WANG, W., LOZANO-DURÁN, A., HELMIG, R. & CHU, X. 2022 Spatial and spectral characteristics of information flux between turbulent boundary layers and porous media. *J. Fluid Mech.* **949**, A16.

WHITE, B.L. & NEPF, H.M. 2007 Shear instability and coherent structures in shallow flow adjacent to a porous layer. *J. Fluid Mech.* **593**, 1–32.

ZAGNI, A.F.E. & SMITH, K.V.H. 1976 Channel flow over permeable beds of graded spheres. *J. Hydraul. Div. ASCE* **102** (2), 207–222.